



Using the Period-Luminosity relation for Cepheid Variable Stars to determine the Distance to the Galaxy Messier-31 (Andromeda)

A. Kimber, L. Shaw, L. Nielsen, R. Haigh, & Y. Wang

School of Physics & Astronomy, University of Edinburgh

Supervisor: Prof. P. N. Best, FRSE

(Dated: November 8, 2024)

Over the course of this report we discuss the infamous Period-Luminosity relation for Cepheid Variable stars. We then observe 11 local Cepheids to verify the Period-Luminosity relation and use it to determine the distance to a 12th Cepheid variable in the Messier - 31 (Andromeda) Galaxy, thus determining an estimate for the distance to Andromeda itself. The relation obtained - $\langle M_V \rangle = (-3.08 \pm 0.27) \log P + (-1.01 \pm 0.25)$ - agrees to within 2σ of the literature Period-Luminosity relation as determined by *G. Fritz Benedict et al.*¹. This was then used to determine a distance to the Cepheid Variable Andromeda-CV1. The value obtained, $825 \pm 106 \text{ kpc}$, agrees with the value obtained by *Adam G. Riess et al.*² - $752 \pm 27 \text{ kpc}$, to within 1σ . However, the error margin on this value is very large.

1. INTRODUCTION

Determining distances to astronomical objects has always been at the forefront of astrophysics and astronomy, with observational methods varying from observing how positions of objects change with viewing angle to measuring how bright these objects look in the night sky. Variable stars, in particular Cepheid Variables, are a prime example of one such method and prove to be very useful in determining distances of up to 30 Mpc, as well as calibrating other distancing methods (especially those that are used to determine distances to the farthest objects in the universe, for example Type 1a Supernovae) on the cosmological distance ladder.

1.1 Historical Significance

Cepheid variable stars were first discovered during the late 18th century by Edward Pigott when he noticed that the star *Eta Aquilae* (formerly known as *Eta Anitnoi*) was displaying variability in its brightness. This information was then passed on to the Royal Society³. A few months later it was John Goodricke who then discovered that the star *Delta* (δ) *Cephei* also exhibited a similar variability and is thus where the term *Cepheid* originates from⁴. Since then the catalogue of known Cepheid variable stars has grown immensely and they have become very important as *standard rulers* due to their well defined periods of pulsation.

1.2 Period Luminosity Relation

During the early 20th century, the infamous relationship between a Cepheid's pulsation period and its intrinsic luminosity was ascertained by Henrietta Swan-Leavitt during her observations of thousands of variable stars within the Magellanic Clouds⁵. This relationship can be seen from the logarithmic plot in figure 1⁶ where the abscissas give the logs of the periods as measured in days and the ordinates are the respective absolute magnitudes.

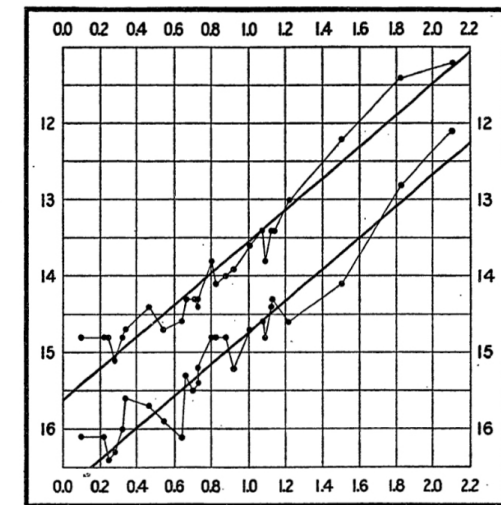


FIG. 1: The apparent relationship between Period and Luminosity from Henrietta Swan-Leavitt's discussion form 1912.

It can be seen that there exists a direct relation between the period of pulsation and the absolute magnitudes (and consequently, the luminosity) of variable stars to within a good degree of accuracy. It can also be noted that the stars observed in her study are all at approximately the same distance from Earth and as a result, the pulsation periods must be directly related to the light emission from the star, which in turn, is determined by their mass and density due to the mass-luminosity relationship. This relationship has become vital in determining distances to some of the most distant astronomical objects due to its simplicity and reliability. Consequently, Cepheid Variables have a pivotal role in the Cosmic Distance Ladder with the ability to determine distances within the Local Group out to as far as 30 Mpc. An approximate Period-Luminosity (PL) relation can be

derived by assuming the period of pulsation is proportional to the free-fall time of the star, i.e.

$$P \propto (G\bar{\rho})^{-\frac{1}{2}}. \quad (1)$$

Where $\bar{\rho}$ is the mean density of the star $\bar{\rho} \propto (\frac{M}{R^3})^{\frac{7}{3}}$. Since Cepheid variables lie on the instability strip of a Hertzsprung-Russell Diagram⁸, their average effective temperature T_{eff} can be considered to be \approx constant. Assuming the radiation output of the stars to be analogous to a black body⁹, it can be stated that $L \propto R^2 T_{eff}^4$ we can state that

$$L \propto R^2. \quad (2)$$

Substituting equation 2 into equation 1 for R it can be seen that

$$P \propto \left(\frac{M}{R^3}\right)^{-\frac{1}{2}} \propto L^{\frac{3}{4}} M^{-\frac{1}{2}}, \quad (3)$$

and since there is a relationship between the mass and luminosity of a star¹⁰ of the form

$$\frac{L}{L_{\odot}} = \left(\frac{M}{M_{\odot}}\right)^a, \quad (4)$$

where L_{\odot} and M_{\odot} are the luminosity and mass of the sun respectively and $1 < a < 6$ (a value of $a = 3.5$ is often used when discussing main-sequence stars¹¹), then it can be seen that there is an intrinsic relationship between period and luminosity

$$P \propto L^{\beta}, \quad (5)$$

where β is a constant.

A more accurate form of the period-luminosity relationship was determined from trigonometric parallaxes of local Cepheid variables using the Hubble Space Telescope (HST)¹

$$\langle M_V \rangle = (-2.43 \pm 0.12) (\log_{10} P - 1) - (4.05 \pm 0.02), \quad (6)$$

where P is the pulsation period in days and $\langle M_V \rangle$ is the time averaged absolute magnitude of the star, given in the V band of the Johnson-Morgan (UBVRI) magnitude system.

1.3 Andromeda and Hubble

The distance to Andromeda (otherwise known as M31 or NGC224), the nearest galaxy to the Milky Way, was first measured by Edwin Hubble, who has often been referred to as the “pioneer of the distant stars”¹², in the late 1920s to be $\sim 275 \text{ kpc}$ ¹³ using the Period-Luminosity relation

discussed in section 1.2. This is quite far off from what we now know to be the distance to Andromeda, lying at a distance of $\sim 752 \pm 27 \text{ kpc}$ from the Earth², although the accuracy is commendable given the limiting technology of the time.

Hubble then went on to use the same Period-Luminosity relation (as well as many other methods) to determine the distances to many other galaxies, measuring their respective recession velocities to derive the infamous *Hubble’s Law*¹⁴, stated originally as

$$v_{rec} = H_0 d, \quad (7)$$

where H_0 is the current value of the Hubble Constant. However, we now know that almost all of Hubble’s measurements proved to be much smaller than the true values, presumably due to different types of Cepheid Variables and discrepancies in determining whether bright objects were gas clouds rather than stars¹⁵.

1.4 Opacity Mechanism

The Eddington Valve, otherwise known as the κ -opacity mechanism is the process by which the pulsation, and hence variability, of Cepheid variable stars originates¹⁶. In this case, κ is a measure of the inability of photons to traverse the stellar atmosphere, and is thus defined as the radiative opacity at an arbitrary distance within the stellar interior.

In most Cepheid variables, if the stellar atmosphere is composed of a large amount of doubly ionised Helium ions, then a large amount of the light released from the core will be absorbed by the Helium ions (meaning the Cepheid is currently in a dimmer state), causing the stellar interior to heat up. This is due to the doubly ionised Helium ions having a greater opacity to singly ionised Helium ions¹⁷, meaning they absorb more light. As the stellar interior heats up, the thermal pressure will increase and eventually overcome the effects of the gravitational pressure, causing the star to expand. As the star expands, the temperature decreases, thus the energy of the Helium ions decreases, which allows the recombination of free electrons in the plasma, creating an abundance of singly ionised Helium. Since singly ionised Helium is more transparent, a greater amount of light is allowed to pass through and thus the star gets brighter. However, this causes a decrease in thermal pressure, and as such the gravitational pressure becomes dominant and the star begins to contract. As the star contracts, thermal pressure and temperature begin to increase, granting the Helium ions more energy and thus returning them to a doubly ionised state, and as a result, the star’s brightness begins to decrease back to its minimum. This process is thus cyclic and therefore the period of these pulsations can be measured through observations of the Cepheid Variables, and as a direct result of the period-luminosity relation discussed in section 1.2, their corresponding luminosities can be measured, which

provides information about the stellar flux of the star and more importantly, the distance to the star.

2. Observation and Image Calibration

A total of twelve Cepheids were observed, eleven belonging to the Milky Way galaxy and one to the Andromeda Galaxy. These can be seen in table I.

TABLE I: Target Objects and their corresponding distances from Earth^a.

Cepheid Name	Distance (pc)
δ Cephei	250
GH Cyg	2150
V438 Cyg	2172
VX Cyg	3322
VZ Cyg	1789
RS Cas	1406
RY Cas	3828
FM Cas	1958
TU Cas	808
DL Cas	1688
RW Cas	3041
SW Cas	2008
Andromeda CV1	T.B.D

^a N.B. The distance to the Cepheid Variable CV1 in Andromeda is determined as part of this project and is thus left as “To Be Determined (T.B.D)”

Unfortunately the first entry (δ Cephei) had to be excluded as, due to it being very bright and very close, the images produced by the PIRATE telescope were over-saturated and thus accurate measurements could not be taken (this can be seen from the finding chart in Figure 2). This star was then replaced by SW Cas (the 12th entry). The remaining eleven were imaged and the data extracted to obtain a period-luminosity relation function, the details of which are outlined in Section 4 and the final Cepheid was imaged in order to derive the distance from Earth to Andromeda (see section 5).

2.1 Finding Charts

The first step of this project was to produce the finding charts for the Cepheids and the Standard Stars. The image and pixel-map extraction functionality via the SuperCOSMOS Sky Survey (SSS)¹⁸ was utilised to create these charts and the parameter selection is outlined as follows: The equinox selected was J2000 as this is the current standard¹⁹; the size of the extracted box was 15 arcminutes and the Survey/Waveband was POSS II Red:

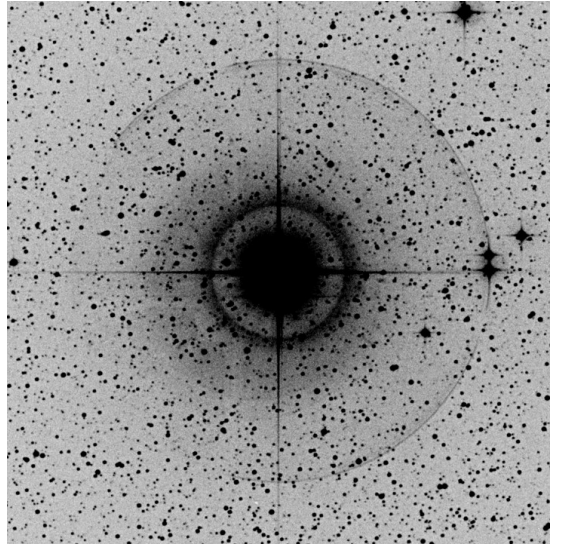


FIG. 2: The finding chart produced for the Cepheid Variable δ Cephei. It can be seen that this star is very bright and very close. Thus the images captured proved to be oversaturated. More on finding charts can be found in section 2.1.

$+2.0 < \text{Dec} < +90$. The Second Palomar Sky Survey (POSS II)²⁰ (Palomar-II Oschin Schmidt Telescope) was used as this would provide finding charts for objects in the northern hemisphere. Despite working with filters closer to the ‘blue’ end of the visible spectrum, the Red waveband was chosen as it provided higher quality and clearer images. The charts were saved in both FITS and GIF image formats for reference on the observation nights.

2.2 Observing with the PIRATE Telescope

Observations of the targets were performed on multiple nights between 29th September and 21st October 2021. These observations were made using the PIRATE telescope located on Mount Teide in Tenerife. As detailed in the Observing Primer²¹, “the main optical component of PIRATE is a 17 inch (43 cm) f/6.8 Corrected Dall-Kirkham Astrograph telescope (a PlaneWave Instruments CDK17). The main imaging camera of the current PIRATE Mk 3 configuration is the FLI ProLine KAF-16803 model with 4096x4096 pixels and pixel size 9 microns. The resulting field of view is 42 arcmin with a pixel scale of 0.63 arcsec per pixel in 1x1 binning.” Prior to these observations, the object visibility was checked for each of the targets using the Isaac Newton Group’s StarAlt planner²². The program provided a useful way of determining which times would be best for viewing each of the targets; ideally they should be observed close to the time of their peak on the object visibility chart as this is when the airmass will reach its lowest value and thus the effects of atmospheric extinction are reduced. Another key consideration was that the altitude of the object at the time of viewing

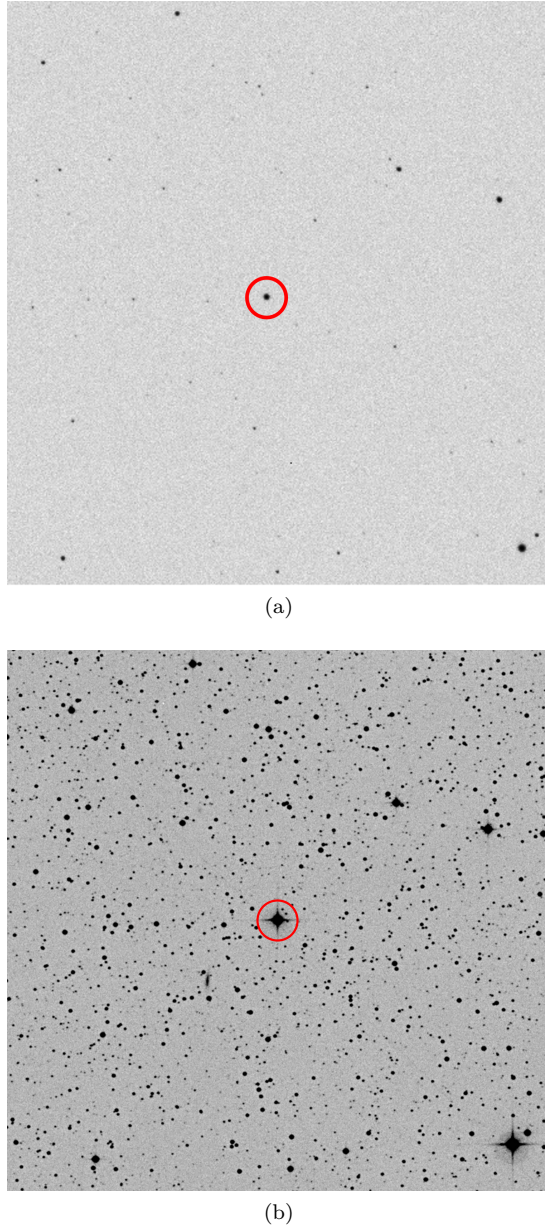


FIG. 3: (a) 180° rotated FITS image of the Cepheid RW Cas as viewed in GAIA. The image is thus centred on the Cepheid and is indicated above. (b) Finding Chart of RW Cas generated by the SSS image and pixel-map extraction function¹⁸. RW Cas can be seen highlighted above.

was required to be above 30° to ensure that the resulting images would be clear and to avoid further complicating the calculation of the atmospheric extinction correction. The telescope was accessed and controlled remotely via Sybilla²³ and schedules were added for each of the targets. These were created on the first night of observation with the required input values including the target object name; Right Ascension (RA) and Declination (Dec) of the target; the filter to be used;

the exposure time; the binning value and the number of repeats. It was highly important that suitable exposure times were chosen for the schedules; if the exposure time is too short, the signal will not be captured sufficiently, resulting in a poor signal-to-noise ratio and thus a poor result. On the other hand, if the exposure time is too long, too much signal can be captured as the flux scales with the exposure time, leading to saturation and also a poor result. Thus, balance must be achieved such that the resultant signal-to-noise ratio is high enough to give a small uncertainty in comparison to the value being measured without saturating the image. The exposure times were tested on the first night of observation and adjusted as necessary.

The schedules were queued on the allocated evenings, ten in total, and the images taken by PIRATE were uploaded to AstroDrive. They were then reviewed frame by frame during the observation session to confirm that all images were clear and of sufficient quality. The finding charts were used to identify the target object in each of the images and the maximum count level of the object was examined to ensure that it was not saturated; in this case, that the count level was below 65,000 to prevent saturation. Any images that did not meet these standards were added to the queue again to be re-run and the successful images were later saved as FITS files.

2.3 Data Reduction

The data reduction aspect of the project concerns the minimisation of the numerous potential sources of contamination in the CCD images. All of the frames necessary for this process were automatically taken by PIRATE each night during the twilight periods, that is dusk and dawn, outside of the observation session and were saved alongside the target object images.

A number of source code files were created with *python 3.8.10* to carry out the computational processes necessary to reduce the raw images taken by PIRATE, thus producing the final images that were used for extracting the data required for this project. These programs make use of a number of different python libraries and modules including *NumPy*, *Astropy*, *OS* and *Argparse*. These processes are explained in further detail in each of the following subsections.

2.3.1 Dark Current

The dark current is one of the three primary instrumental signatures of the CCD; it consists of the electrons that are generated by the detector itself through thermal radiation²⁴. In order to account for this, dark frames must be taken with the shutter of the CCD closed such that zero photon-induced electrons will be counted and thus the only electrons accounted for will be the dark current²⁵. Generally, the dark frames would be taken and stacked in a similar manner to the way in which the other instrumental signatures are processed and handled. However, the FLI Proline CCD used by

PIRATE can be cooled to 70° celsius below the ambient temperature^{26,27}, hence the detector is cooled sufficiently such that the dark current can be considered negligible. This was confirmed using original source code created with *Python 3.8.10* in which the mean values of the pixel elements of both the dark frames and the bias frames were compared. The bias frames were found to have an average value of 978 ± 9 while the dark frames had an average value of 977 ± 21 . It can be seen that these averages are extremely close in value such that there is no clear difference in the dark frames and thus the dark current in this case could be disregarded.

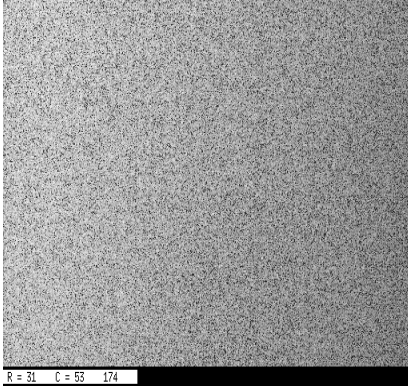


FIG. 4: Example of Dark Current frame^a

^a N.B. Since the PIRATE dark current was negligible, this is not an original frame.²⁸

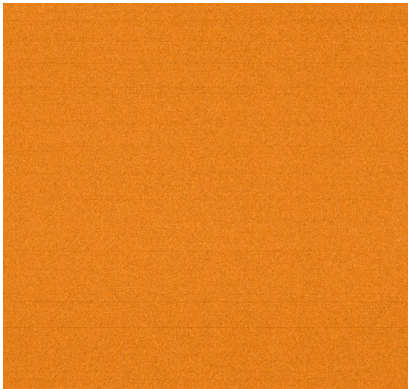


FIG. 5: Example of the Bias frame, taken from PIRATE's calibration frames on 29 September 2021.

2.3.2 Bias

During the process of producing an image, there are a number of steps that must be taken to convert the photo-electron charge to a voltage signal which is then used by the Analogue-to-Digital Converter (ADC) to provide the imaging software with a count value for each pixel²⁹. Inherent noise is generated throughout this process across the different steps and the sum of the noise is referred to as "readout-noise."³⁰ It is possible for

the readout-noise to generate a negative signal which is then received by the ADC, however, this is not ideal. Thus, to ensure that this does not occur, the CCD is set up in such a way that a negative value cannot be returned by adding an offset, otherwise known as the bias. Consequently, even without the recognition of photo-electrons or thermally induced electrons, the pixels will not register a count value of zero²⁵. Therefore, the counts returned in the raw CCD images must be calibrated such that this offset is accounted for. Bias frames are similar to the dark frames in the sense that they are also taken with the shutter closed so that there is no light incident on the CCD. In addition to this though, bias frames must be taken with an exposure time as close to zero as the CCD and imaging software will allow. The reason for this is to ensure that only the base-level noise from the bias is captured as the possibility of capturing the noise from the dark current is minimised.

As mentioned previously, the calibration frames were taken automatically by PIRATE and saved in the form of FITS files. As the target object images were taken with a 1×1 value for the binning, the calibration frames must also possess the same binning value. However for a number of the calibration frames, this was not the case. As multiple bias frames were taken each night, original source code using *Python 3.8.10* was used to determine the binning of the frames and stack each of the suitable frames in order to increase the signal-to-noise (SN) ratio. Ten different master bias frames were created, one for each night, comprising of the frames from the respective night. The code incorporated *NumPy*'s functionality to set the counts of each pixel to a 2D-array and find the median value of the same element in every frame. Additionally, these master bias frames were stacked to find the mean count and the standard deviation of the bias across all of the nights, which were determined to be 979 ± 3 . The mean count of the individual bias frames were all found to fall within this range and so were all deemed suitable for use. The raw images taken by the CCD were bias-subtracted using the corresponding master bias frame from the observing session that the images were taken.

2.3.3 Flat-Field

Ideally in a CCD, a single photon would give rise to a single photo-electron and that would lead to the recognition of a single count³¹. However, as with all electronics, CCDs do not perform every operation with 100% accuracy and as such there are variations from pixel to pixel in their sensitivity. In addition to this, dust and dirt on the lens can obstruct the view and vignetting can occur, where the brightness of the image is decreased around its edges. In order to account for this, flat-field images must be taken. This involves taking an image of a light source with as little variation in the brightness as possible such that these obstructions can be clearly discerned and differentiated from any fluctuations in the

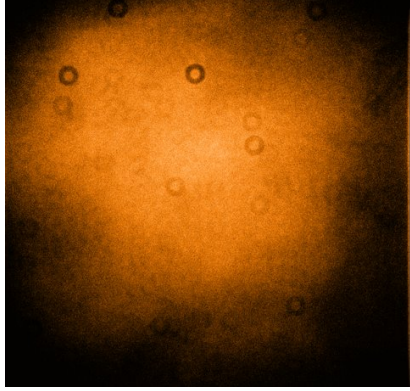


FIG. 6: Example of the Flat-field frame, taken from PIRATE’s calibration frames on 29 September 2021.

source radiation²⁵. There are two different approaches to taking flat-field images, dome flats and twilight flats, and PIRATE automatically takes the latter during dusk and dawn outside each observing session²¹. The flat-field images are taken during twilight, between the setting and rising of the Sun, as the sky is well lit but not so bright that the count level will be saturated. The variations in the pixel sensitivity also differ with respect to the wavelength of the incoming light and thus it is necessary to capture different flat-field images for each of the filters that will be used for the target object images. Prior to any processing of the flat-field frames, the frames were bias-subtracted using the master bias frame from the same observing session as each of the flat-field frames. Similarly to the calibration of the bias, original source code in *Python 3.8.10* was used to find the binning of the flat-field frames and *NumPy* was incorporated to calculate the mean count of each of the suitable frames so that every pixel in each of these frames could be scaled such that the different frames had the same mean count level. A total of 9 flat-field frames in the V-filter and 15 frames in the B-filter were determined to have a binning of 1x1 and thus were determined suitable for use in this process. The flat-field frames were set to a 2D-array and the V-filter frames were stacked by finding the median of each element across the frames. Following this, the V-filter master flat-field frame was created by dividing the elements of the stacked frame by their mean value in order to normalise this frame. The same procedure was also carried out to produce a master flat-field frame in the B-filter.

2.3.4 Finalisation

The final step of the data reduction process, after subtracting the bias and dividing by the flat-field, was to normalise the calibrated target object images³². The images had already been set to 2D-arrays in order to execute the previous steps of the data reduction process and in order to normalise them, the arrays were divided by their exposure time which was extracted from the headers of

the FITS files using *NumPy*. The target object images were now calibrated and ready for the necessary data to be extracted. An example of a before and after reduction procedure can be found in figure 7.



(a)



(b)

FIG. 7: (a) FITS file of RW Cas before any of the reduction process (b) FITS file of RW Cas after being fully reduced with higher signal-to-noise ratio

3. STANDARD STARS

Standard Stars play a key role in the process of data calibration; they allow for the instrumental magnitudes measured by the CCD to be converted into observed magnitudes within the chosen photometric system, thus providing a context for the data in which it is meaningful. Upon completion of this calibration, the data can be utilised to infer a number of intrinsic properties of the target objects. In this particular project, we worked with the B, V and G passbands of the Johnson-Cousins system³³. Standard Stars also provide us with a way of accounting for atmospheric extinction and the two main approaches to this will be discussed in further detail below (see section 3.3).

3.1 Selection of Standard Stars

Generally, it is considered the case that “calibrators should occupy a similar volume of parameter space as the things which they are calibrating.”³⁴ There are a number of criteria that Standard Stars should meet in order to perform well in terms of this calibration.

The first of these criteria is that the span of the altitudes, and thus airmasses, should encapsulate that of the target objects³⁴. The altitudes of the Cepheids were between 35° and 85° while those of the Standard Stars were between 31.3° and 75.4° with corresponding airmass values of 1.99 and 1.04 respectively. Thus, the Standard Stars spanned across a range of approximately 1 airmass which would be sufficient for this project.

The second criterion is that the “celestial coordinates”³⁴ of the Standard Stars should also be similar to those of the target objects. Of course, the RA must be similar so that the stars can be viewed during the same time period, i.e. at the same time of year, and the Dec must be similar in order to meet the first criterion. The RA of the Standard Stars ranged from a value of $\alpha = 16^{\circ}47'23.224$ to $\alpha = 00^{\circ}46'34.507$. The RA of all target objects, with the exception of one, *RW Cas* with a value of $01^{\circ}37'14.02$, fell within this range.

The third and final of these criteria is that the magnitudes and colours of the Standard Stars should resemble (“or be slightly larger than”³⁴) those of the target objects. The magnitudes must be large enough that it is easy to observe the Standard Stars but not so bright that the count levels exceed the limit of saturation³⁵. The Standard Stars selected in this project were chosen such that their magnitudes in the V-band were between 10 and 12, with a maximum magnitude value of just under 13 in the U-band.

The Standard Stars were chosen from Landolt (2013)³³. A number of potential Standard Stars were investigated before narrowing down to the four selected. The initial set of Standard Stars were chosen based on the magnitudes in the V- and U-bands as well as their RA values. Upon selecting a variety of Standard Stars that met both criteria 2 and 3, the object visibility functionality (see section 2.2) was incorporated to review their altitudes and airmass values on the first night of observation, leading to the selection of the final four Standard Stars.

3.2 Aperture Photometry

When performing aperture photometry and selecting an aperture size, there is a careful balance to be struck between ensuring the aperture is large enough to capture as much of the flux from the target as possible and that the aperture is small enough that the noise from the sky background is minimised. In order to conclude which size of aperture should be used, the standard stars were all reviewed in *GAIA* (*Graphical Astronomy and Image Analysis Tool*), “an image and data-cube display and analysis tool for astronomy”³⁶. The slice functionality was used to generate a 1D profile of the pixel values of

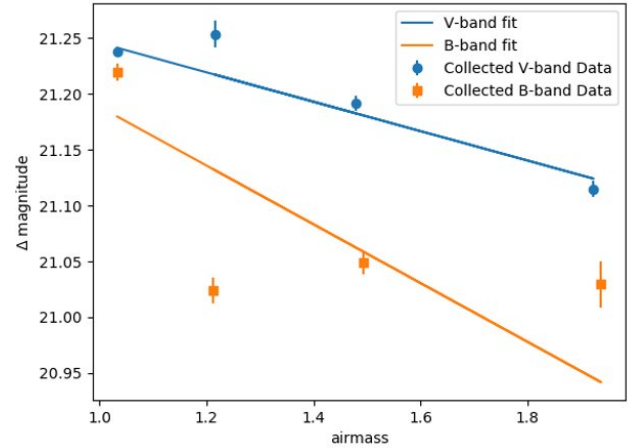


FIG. 8: Plot of Δm against the airmass, where m_{zero} is the y-intercept and $-\kappa_\lambda$ is the gradient.

the star and from this plot the Full Width Half Maximum (FWHM) was determined. An aperture size of 3 times the FWHM was selected as a good compromise as this diameter captured approximately 90% of the total signal of each of the stars. Using the chosen aperture size, the instrumental magnitudes of the standard stars were calculated with the aperture photometry function in *GAIA*.

3.3 Zero Points and Atmospheric Extinction

With the instrumental magnitudes calculated, it was now possible for the standard stars to fulfil their purpose as outlined in the introduction of this section. In order to make sense of the data gathered on the Cepheids, the instrumental magnitudes must be converted onto a standard system; in this case, the Vega system as the Johnson-Cousins photometric system is based upon this³⁷. This conversion can be carried out using the formula,

$$m_{vega} = -2.5 \log_{10}(C) + m_{zero} - \kappa_\lambda \sec \theta, \quad (8)$$

where m_{vega} represents the ‘true’ magnitude, m_{zero} the zero point magnitude, κ_λ the extinction coefficient, $\sec(\theta)$ the airmass and the instrumental or observed magnitude is defined as,

$$m_{obs} = -2.5 \log_{10}(C). \quad (9)$$

However, to determine the magnitude on a standard system, the zero point and extinction correction coefficient must be known. Using the instrumental magnitudes from our own observations of the standard stars as well as the pre-existing and well-defined literature values of the ‘true’ magnitudes³³, these terms could be ascertained. Utilising the *Astropy* functionality within *Python 3.8.10*,

the altitude of each of the standard stars were extracted from the image headers in both the B- and V-filter and then combined with the following equation to derive the airmass,

$$\sec \theta = \frac{1}{\cos(90 - \alpha)}, \quad (10)$$

where in this instance, a represents the altitude of the target object. If equation 8 is re-arranged and combined with equation 9 like so,

$$m_{vega} - m_{obs} = m_{zero} - \kappa_\lambda \sec \theta, \quad (11)$$

a linear relation can be seen between the airmass and the difference in magnitudes where m_{zero} represents the intercept of the y-axis and $-\kappa_\lambda$ represents the gradient. The plot in figure 8 shows this relation for each of the filters used and from this, the necessary values can be derived. Concluding this stage of the project, the zero points were determined to be $m_{zero} = 21.180, 21.259$ and the extinction coefficients to be $\kappa_\lambda = 0.257, 0.231$ for the B- and V-filter respectively.

4. CEPHEID VARIABLES

Given the vast number of images and thus the substantial mass of the data that had to be processed, a software named *Source Extractor* was opted for to perform the aperture photometry of the targets. *Source Extractor* creates a catalogue of all the objects in an image based on the parameters and thresholds selected by the user in the parameter configuration file. This software was used to create a catalogue of objects for each of the CCD images taken across the ten nights of observations. Most of the parameters maintained the default values of the program. The parameter values that were adjusted include the aperture radius which was set to a value of 20 pixels, the minimum detection area to 5 pixels and the analysis threshold to 10 magnitude per arcsecond squared. Thus, for an object to be recognised as such by the software, it would have to be at least as bright as 10σ above the background noise across a minimum of 5 connected pixels. Any object that met this criteria would then be added to the catalogue.

4.1 Comparison Stars

In order to identify the target within the object catalogues, four comparison stars were chosen from the Cepheid CCD images taken on the first night of observation. A single frame was viewed in *GAIA* for each of the Cepheids and the four stars were selected such that they were highly distinguishable, non-variable, luminous and in different quadrants of the image. The positions of these comparison stars, as well as the Cepheids, were

recorded in an excel file which would later be accessed by *Python 3.8.10* code to find these targets within the corresponding catalogues and isolate the data from these specific objects. There are two stages to the extraction of the necessary data.

In the first stage, the catalogues for the images which the comparison stars were chosen from, are accessed by the code, which combs through all of the objects to find those with the smallest difference in the coordinates such that

$$\min|\delta(x, y)| = \min|(x_{SE} - x_{GAIA}) + (y_{SE} - y_{GAIA})|. \quad (12)$$

Having determined the catalogue object closest in value of the coordinates to those recorded manually using *GAIA*, the code then created a unique map by calculating the position vectors of the comparison stars with respect to the position of the Cepheid. An example of one of these vector maps can be seen in figure 9.

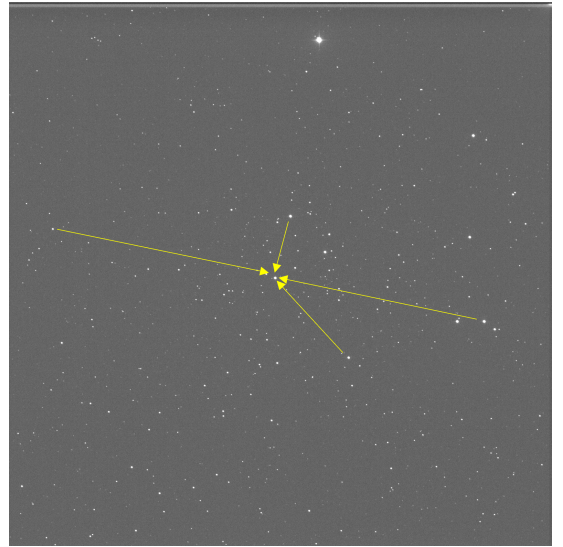


FIG. 9: A representation of a vector map created for the Cepheid Variable DL Cas, with the position vectors in yellow.

The second stage concerns the identification and extraction of the comparison stars and Cepheids from the remaining catalogues. The vector maps were applied to these catalogues and looped over all of the objects until the five targets were returned from each corresponding catalogue. In the case of images that had been taken such that they were rotated 180° , due to the meridian flip³⁸, the coordinates, and thus position vectors, of the comparison stars could not be determined. To correct this, the coordinates of the comparison stars in the flipped images had to be manually recorded, again using *GAIA*, and added to the excel file. The code was altered such that the process to create the position vectors was executed for these new coordinates in addition to the originals, resulting in two vector maps. In the absence of

the code being able to find the targets using the initial vector map, the secondary map was used and thus the comparison stars and Cepheids were extracted from every catalogue.

4.2 Magnitude Calibration

This step of the project also consisted of two stages, in which the magnitudes of the targets were calibrated but the method of doing so was different for each stage. The first magnitudes to be calibrated were those from the first night of observing. The magnitudes of each of the Cepheids and their comparison stars were converted from the instrumental magnitudes provided by *Source Extractor* to *Vega* magnitudes using the previously determined zero point m_{zero} and atmospheric extinction coefficient κ_λ for the V-filter³⁹. The altitude of the Cepheid was taken from the header of the given image using *Astropy* and used to determine the airmass using equation 10. Combining these values with equation 11, the *Vega* magnitudes of the comparison stars and the Cepheids were determined for each of the frames taken on the first night. For the remaining data from the nine subsequent observing sessions, the calibration values were not available as the standard star images had only been captured on the first night. Thus, in order to execute the magnitude conversion, the instrumental magnitudes of the comparison stars from the subsequent nights were compared with those from the first night. Since the comparison stars are non-variable, the difference in magnitudes across observing sessions would have been due to differences in the atmospheric extinction. Calculating the differences in their magnitudes allowed an offset value to be determined which could be added to the magnitudes of the Cepheids in order to account for the atmospheric extinction and thus derive the magnitudes of the Cepheids. This process of finding the variance in magnitude was carried out for each night. The average value of the comparison star magnitude difference was taken across the four stars and across the five frames of each Cepheid, providing an offset value which could then be added to the magnitude of the Cepheid on the corresponding night. Hence, there were five magnitude values for every Cepheid on each of the different observing nights. These five magnitudes were averaged, resulting in a total of ten different magnitude values for each Cepheid across the observing timeline. The mean magnitudes for each night were then plotted against observing time as can be seen in figure 10.

It should be noted that according to the literature values of the periods of some of these Cepheid Variables⁴⁰, there are multiple periods within this data set and due to only observing on ten nights out of the twenty-two night period, there may be *missing data* such as the large “flat” areas on some of the lines (e.g. the area between 4 and 15 days for the TU Cas Cepheid). This means that the data must be folded back such that all the points lie within one pulsation period.

The uncertainties on each of the average magnitude val-

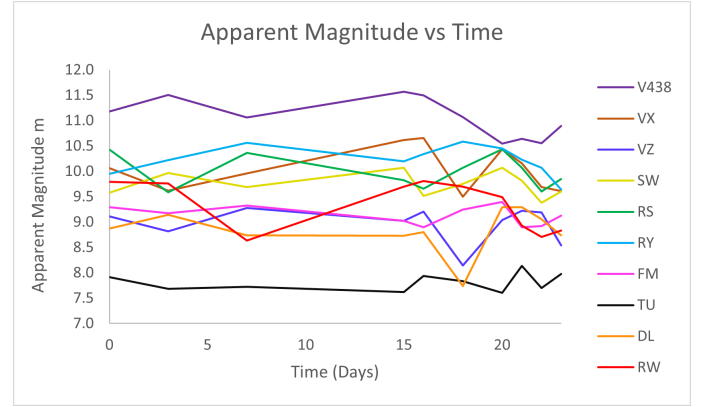


FIG. 10: A plot of the apparent magnitude measurements against observing time for each Cepheid Variable^a.

^a N.B. The Cepheid GH Cyg has been excluded here due to issues with the data, for more information see section 4.3.

ues were derived using the standard deviation σ ,

$$\delta m = \frac{\sigma}{\sqrt{n}}, \quad (13)$$

where n represents the number of measurements, which in this case was $n = 5$. During the data analysis phase, it became clear that these values of the uncertainty were underestimated. The Chi Square values that were calculated, detailed in 4.3 were much larger than would be expected, possibly due to errors being small, so it was decided that a minimum uncertainty of 0.1 would be set. Due to the imperfect process of flat-fielding and bias subtraction, it was concluded that it was reasonable to expect an error of this degree.

4.3 Derivation of the Period

To obtain the period of each Cepheid, first a light-curve must be fitted to the data points of the observed apparent magnitude against time. In this project, a simple fit of a sine curve and a simple sawtooth light-curve were used. Source code in *Python 3.8.10* was utilised to plot the data points and fit the curve. Initially, possible values for the period of the Cepheid were tested by looping over these values, in increments of 0.1, from 1 to 23 (the length of time over which observations were taken). For each of these values for the period, a sine curve was fitted using,

$$y = A \sin(\omega x + p) + c, \quad (14)$$

where A is the amplitude of the curve, ω is the angular frequency, p is the phase and c is the offset. Calculating the angular frequency from the derived value of the period;

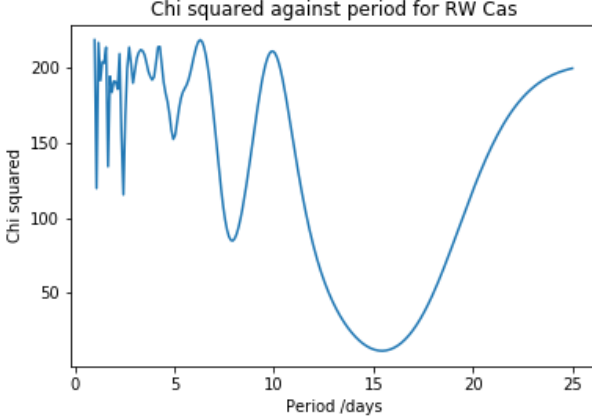


FIG. 11: Chi-square - period plot for Cepheid RW Cas

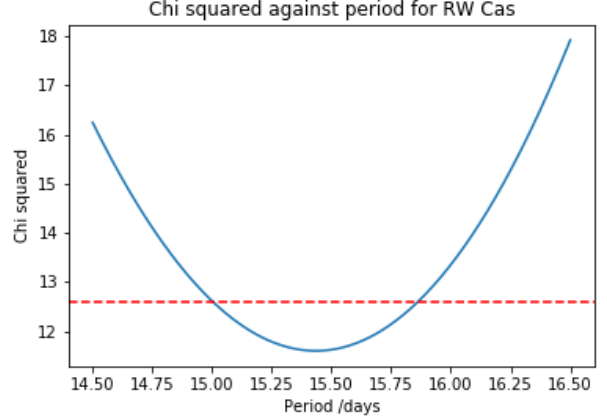


FIG. 12: χ^2 - period plot for Cepheid RW Cas with $\chi^2 + 1$ line (68% 1σ confidence interval) marked in determining the uncertainty on the minimum χ^2 value

$$\omega = \frac{2\pi}{\text{period}}. \quad (15)$$

Scipy's optimize function, which uses a non-linear least squares fit, was employed to find the best fit of the sine function to the data, obtaining the optimal values for A, p and c with their respective ω value. For each of these fits, χ^2 was calculated using,

$$\chi^2 = \sum \frac{(O - E)^2}{y_{\text{error}}^2} \quad (16)$$

to compare the fit with the data and therefore determine whether it was a reasonable fit. A plot of χ^2 against the period was produced in order to clearly identify the period at which there was a minimum value of χ^2 as this was likely to be the period of the Cepheid.

Given the degrees of freedom $v=8$, in order to obtain a reasonable goodness of fit and a best-fit reduced χ^2 of 1, a minimum χ^2 value of approximately 7-8 would be expected. From Figure 11, it is clear to see that the value for the χ^2 is slightly higher in comparison. This could be attributed to an underestimation of the uncertainties on the apparent magnitude values. It is also possible that a sine curve does not provide a perfect explanation of the data and the values would benefit from a more complex light curve fit. So while the obtained values were slightly higher than expected, they would not be deemed unreasonable.

Using a 68% significance level and given that there is only one parameter for the fit, a straight line at $\chi^2 + 1^{41}$ was plotted to determine the uncertainty on the value for the period. This provided a visual on the acceptable values within the minimum dip in the χ^2 period plot, as seen in Figure 12.

Using this period, the data points were folded back over, such that one complete cycle was obtained for the

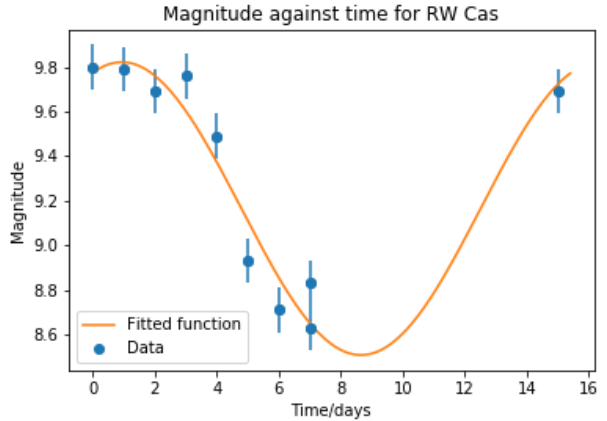


FIG. 13: Sine curve fit to RW Cas data points, Apparent Magnitude against Time

Cepheid and the period obtained from the minimum χ^2 was used to fit the sine-curve. From this, it can be seen whether the derived value for the period is a suitable result. In the case that the fit does not look accurate, a second or third minimum from the χ^2 period plot can be used to refit it.

In some instances, the sine-curve was not an optimal fit for the data. To improve the results, a sawtooth was fitted to each of the Cepheids and results were compared to determine which fit was best for each of the Cepheids. To fit the sawtooth, the data points were folded back over one period and two straight lines of opposite gradient were plotted.

Figure 14 shows a sine curve fit and a sawtooth fit for SW Cas. Comparing these fits, it is clear that the sawtooth fit is much more appropriate for the data.

While it was possible to obtain reasonable light curves for most of the Cepheids, the decision was made to exclude GH Cyg as both the sine and sawtooth fit were not a

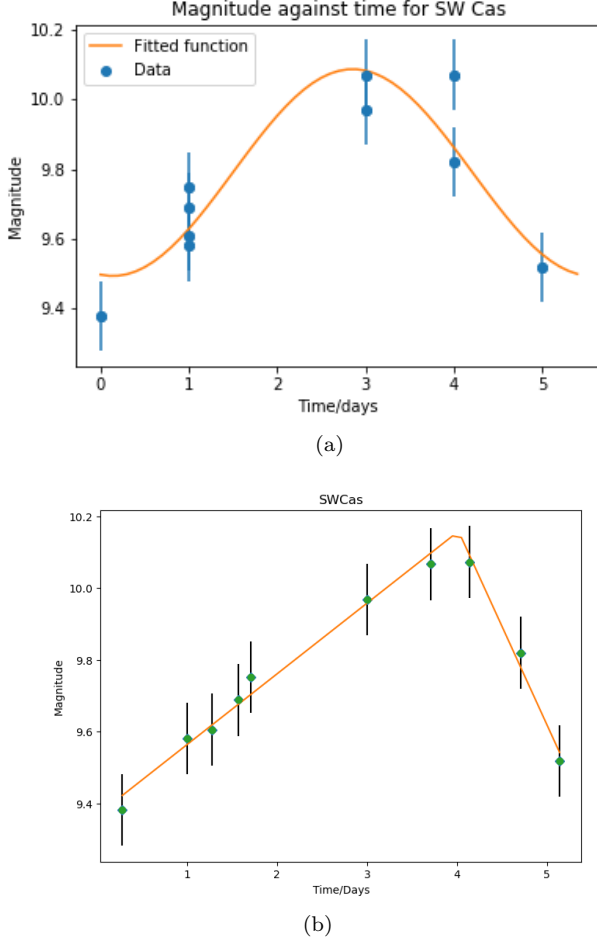


FIG. 14: (a) Sine curve fit for SW Cas (b) Sawtooth fit for SW Cas

good fit for the data and therefore accurate results could not be obtained for this Cepheid. Figure 15 shows the sine curve and sawtooth fit for *GH Cyg*, where it is clear that the light curves do not fit the data. This is also apparent from the χ^2 values as the minimum χ^2 value is approximately 130, which is much larger than would be expected, showing that the fit is not suitable.

Having now fit a light curve to each of the Cepheids, from these fits the mean of the curve, and therefore the mean apparent magnitude of each of the Cepheids, could be determined.

Each of the values for the periods and the mean apparent magnitudes were compared with literature values⁴⁰.

See Appendix A for the χ^2 plots and light curve fits for each of the Cepheids, and Appendix B for a complete table of values.

4.4 The Period-Luminosity Relation

The observed values of mean magnitude that were obtained for each Cepheid required interstellar extinction correction, which involved subtracting A_V from the mag-

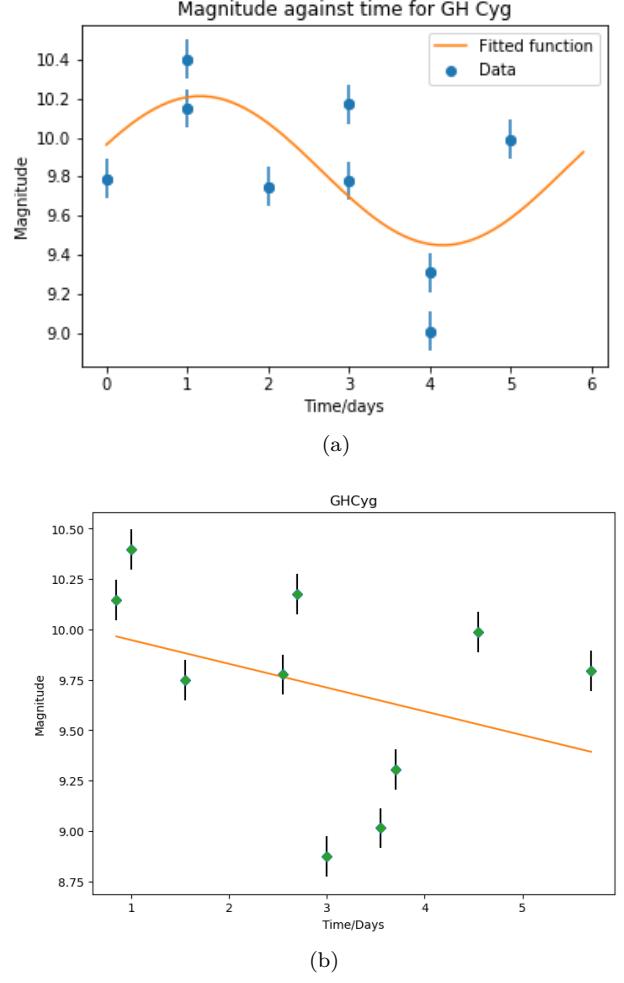


FIG. 15: (a) Sine curve fit for GH Cyg (b) Sawtooth fit for GH Cyg

nitudes, where A_V is calculated using the equation,

$$A_V = R_V E(B - V), \quad (17)$$

where a Milky Way extinction curve⁴² was used, taking a typical value for the diffuse interstellar medium as $R_V = 3.1$, in addition to the corresponding E(B-V) values for each Cepheid, taken from⁴³. Using these corrected values and the known distances to each of the Cepheids (from Table I) the distance-modulus equation,

$$M_V = m - 5 \log_{10} \left(\frac{d}{10pc} \right), \quad (18)$$

was used to determine the absolute magnitude of each Cepheid. As the absolute magnitude is proportional to the log of the luminosity, these values for the absolute magnitude were then plotted against the log of the period, to produce a period-luminosity plot as seen below

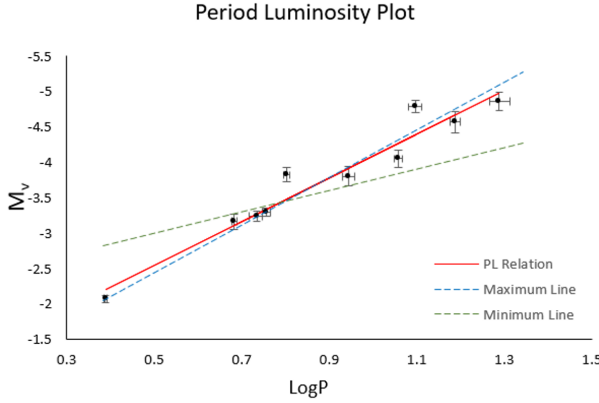


FIG. 16: Period-Luminosity plot displaying 10 Cepheids, a line of best fit and a max and min line

in Figure 16.

At first glance it appears that this is the result that would be expected; it looks comparable to the Period-Luminosity relation in Figure 1. A line of best fit was plotted, using the least-squares technique, that can be seen in Figure 16 and the equation of that line was determined to be

$$\langle M_V \rangle = (-3.08 \pm 0.27) \log P + (-1.01 \pm 0.25). \quad (19)$$

Lines of maximum (blue) and minimum (green) gradient were also fit to the data and are represented by the dashed lines shown above in figure 16. It can be seen that most of the points lie within the area enclosed by the maximum and minimum lines, suggesting that the straight line fit (red), is appropriate. It should be noted that there are two points that exist outwith this region, however, they do not lie too far from the line of best fit and thus have not been considered as outlier points. It is also worth noting that the error bars appear to be very small, suggesting underestimation of errors. A corresponding residuals plot was made for the Period-Luminosity relationship and is shown in figure 17.

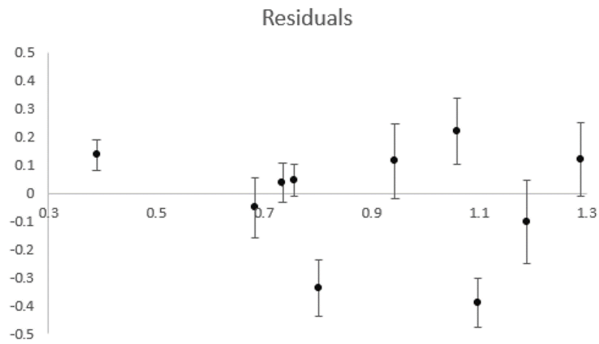


FIG. 17: Plot of the residuals of the Period-Luminosity relation shown above in figure 16.

It can be seen that the scatter of the error bars seems reasonable and is what would be expected, with roughly the same number of points below and above the $\log P(x)$ axis. However, most of the points lie outwith a single error bar implying that the errors have been underestimated.

5. ANDROMEDA

This section details how the Period-Luminosity relation derived in the previous section was applied to a combined dataset of the Cepheid $V1$, which lies on the outer edge of the Andromeda galaxy, in order to determine the distance between Earth and Andromeda. This dataset consisted of data gathered using the PIRATE telescope and provided data captured with the Liverpool Telescope (LVT) in La Palma, Spain. PIRATE captured images of $V1$ on two out of the ten nights, including the first night when the images of the standard stars were taken. However, this Cepheid was imaged in both the B- and V-filters which would later allow the magnitudes to be converted onto the photometric system used in gathering the LVT data.

5.1 Magnitude Calibration

The first step in analysing the Andromeda data was to correct the magnitudes to account for atmospheric extinction. A similar approach as explained in section 4.2 was taken, such that the images of Andromeda from the first night were viewed in *GAIA* to select four non-variable comparison stars and their positions were noted. The magnitudes of the Cepheid and the comparison stars were calibrated in both the B- and V-filter using the relevant zero points m_{zero} and extinction coefficients x_λ from section 3.3, in addition to the altitude of the target which was taken from the header of the image using *Astropy*. Equation 10 was used to calculate the airmass and the calibrated magnitudes were determined using equation 11. Having calculated the ‘true’ magnitude values of the comparison stars, these could now be compared to the instrumental magnitudes of the same stars in the CCD images from the second night Andromeda was observed, allowing two offset values to be derived for the atmospheric extinction in each filter. These offsets were then combined with the instrumental magnitudes of $V1$ to give the calibrated magnitudes. These magnitudes were used to determine the (B-V) colour,

$$B - V = m_B - m_V, \quad (20)$$

which was then combined with the following equation to convert all of the magnitudes from the Johnson-Cousins system to the g-filter within the ugriz⁴⁴ system,

$$g = V + 0.6(B - V) + 0.12^{45}. \quad (21)$$

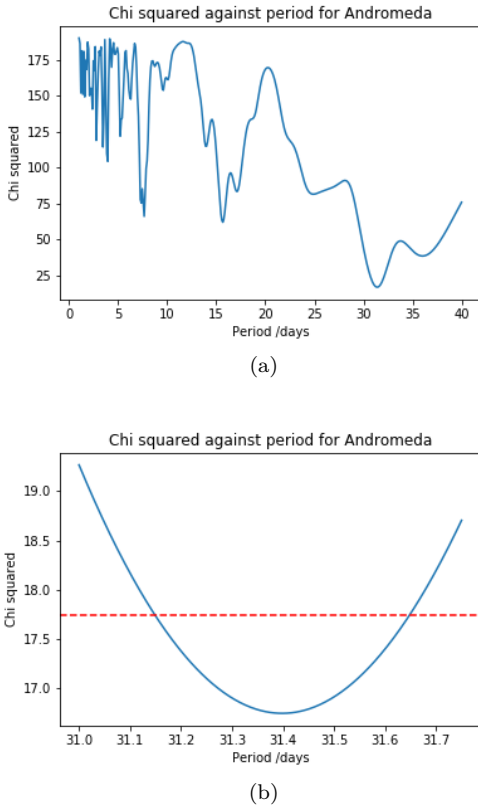


FIG. 18: (a) χ^2 -Period plot for $V1$ in Andromeda (b) χ^2 -Period plot focused on minimum χ^2 , showing $\chi^2 + 1$ line determining the uncertainty at 1σ (68%) confidence interval

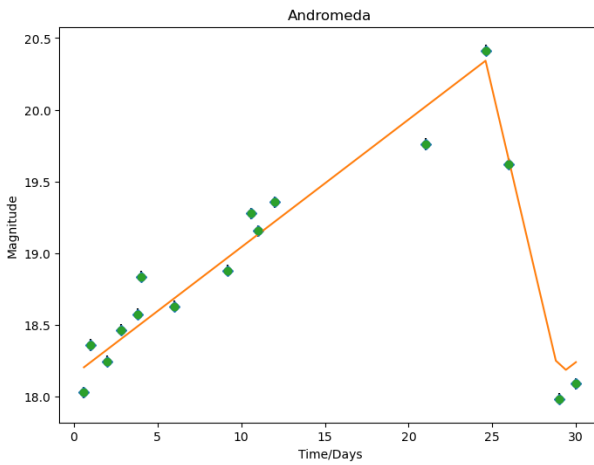


FIG. 19: Sawtooth fit for $V1$ in Andromeda

With all of the data in the context of the same filter, *Source Extractor* was implemented again to create catalogues of the data from the LVT. Original source code in *Python 3.8.10* was utilised to create a vector map of the comparison stars with respect to $V1$ and the five targets were extracted from the LVT catalogues. As the LVT had already undergone data reduction, the only calibration required was that of the atmospheric extinction. The same method was applied such that the differences between the comparison star magnitudes in the LVT images and the image of $V1$ from the first night were used to find the ‘true’ magnitude of the Cepheid from the LVT observing sessions. All of these magnitudes were then converted back to magnitudes in the V-band using equation 23 and used to derive the period of $V1$.

5.2 Derivation of the Period

To determine the period for the Cepheid Variable Andromeda $V1$, the same method as used for the ten local Cepheids was implemented as outlined in section 4.3.

The period as determined by the minimum χ^2 plot was

$$P_{V1} = 31.40 \pm 0.25 \text{ days.} \quad (22)$$

Since Andromeda $V1$ exhibits periodic behaviour analogous to a sawtooth and unlike a sine curve, a sawtooth with a period of 31.4 days was fit to the data, as shown in Figure 19, from which the mean apparent magnitude was determined to be 19.15.

5.3 Determining the Distance

Using the period obtained in section 5.2, the Period-Luminosity relation derived from the measurements of the ten local Cepheids from section 4.4 and the mean apparent magnitude attained from the sawtooth fit, the mean absolute magnitude in the V-Band was determined to be,

$$M_{V_{CV1}} = -5.6191 \pm 1.5650. \quad (23)$$

This can be seen plotted onto the Period-Luminosity relation from 4.4 in Figure 20.

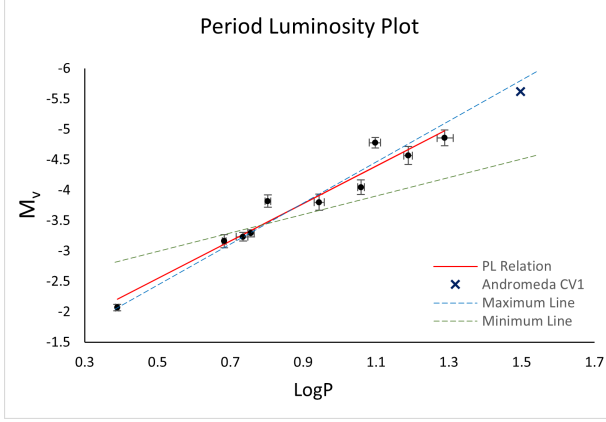


FIG. 20: The Period-Luminosity relation from 4.4, with an added point for Andromeda V1 marked by the ‘X’.

Using this value and the mean apparent magnitude extracted in section 5.1, the distance could then be calculated using the distance modulus equation as presented in equation 18. This yielded a distance of

$$d_{\text{Andromeda}} = 825 \pm 106 \text{ kpc}, \quad (24)$$

where the errors have been folded through from the errors determined for equations 19, 22, and 23 using standard error propagation techniques,

$$\delta d = \sqrt{\delta m^2 \left(\frac{\partial d}{\partial m} \right)^2 + \delta M^2 \left(\frac{\partial d}{\partial M} \right)^2}, \quad (25)$$

which, using equation 18, yields

$$\delta d = \frac{d \ln 10}{5} \sqrt{\delta m^2 - \delta M^2}. \quad (26)$$

Comparing this to the known literature value for the distance to Andromeda of $752 \pm 27 \text{ kpc}^2$, it can be seen that the distance derived is quite far off but still within one error margin (1σ) due to a large error on the distance ($\sim 12\%$).

6. DISCUSSION

First, it should be noted that during the observations, the PIRATE telescope dome had to be closed numerous times due to moisture from the low cloud base, thus causing images to exhibit blurring. At the time of observing the cloud base was required to be above 2700m for the dome to be able to open without risking damage from moisture. This can be seen in Figure 21, allowing the ability to plan ahead and watch the trends that the cloud base was following. This also meant that there was a waiting time for imaging more of the targets and

this caused some of the Cepheid Variables to move closer to the horizon, thus exhibiting more atmospheric extinction. Likewise, it should be mentioned that the weather is unpredictable and due to the PIRATE telescope being ground-based, the clouds can cause a lot of blurring in the images produced, leading to anomalies in the data. This was especially the case on one night as, at the time of observing, the Cumbre Vieja volcano on La Palma, a neighbouring island to the PIRATE telescope in the canary islands, had been erupting since the beginning of September, causing heavy ashfall on multiple nights that were intended to be used for observing. The PIRATE telescope’s dome was shut for the entire duration of these nights and thus extra data was missed out on.

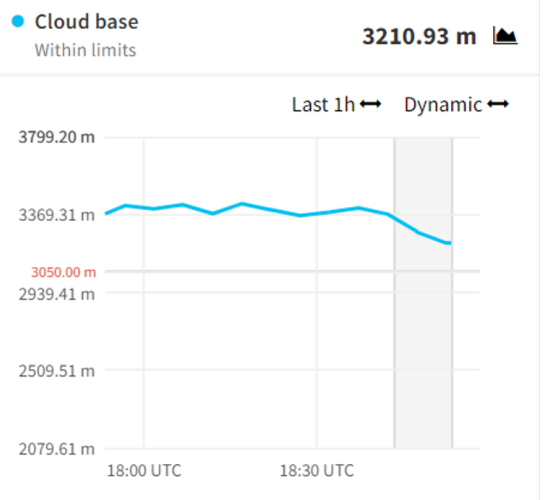


FIG. 21: A plot of cloud base height against time as provided by the PIRATE telescope

The PIRATE telescope also had limited usage time as it is not the property of the University of Edinburgh School of Physics and Astronomy, but rather that of the Open University. Therefore, only a small number of observations could be taken due to time constraints, meaning there was limited data to work with when deriving the Period-Luminosity relation and the distances to Andromeda.

Finally, the dark current from the PIRATE telescope was neglected as the telescope is cooled to a sufficiently low temperature, causing the influence to be negligible. However, there could still be a small variation due to this and thus if it had been taken into account, the values for the mean magnitudes and periods may have differed slightly. Although it is likely that this difference would also be negligible.

6.1 Cepheid Variable Results

The values for the mean magnitudes and periods determined by the data gathered by the PIRATE telescope, appear to agree with known literature values provided by the Variable Stars Index⁴⁰, all to within 1σ . However,

the errors on these values are significantly small, which is unexpected due to the large amounts of blurring on the images and the slight altering of positions between the images. This is because the software packages, like *GAIA* and *Source Extractor*, take the number of counts calculated, and by using Poisson statistics, convert that value into an uncertainty. However, this is a lower bound due to the fact that the packages assume that the data reduction process has been flawless. In reality, the errors are larger due to errors made in data reduction such as imperfect flat fielding or background subtraction. Other factors that contributed to the uncertainty values include the time the telescope took to open and close its shutters and the inherent uncertainty in imperfect technological operation execution. To get a better estimate for the uncertainty, for any image, a number of 5 arc second apertures would have been placed at random positions on the background of the image and the counts would have been measured. This would form a Bell curve, with a mean value of zero but a width of 1σ of the counts, providing a more accurate value for the uncertainty. This wasn't done however due to the time constraints on the report. The Period-Luminosity relation appears not to agree with the literature, with the gradient being $\sim 2\sigma$ out from the value determined by *G. Fritz Benedict et al.* and the Hubble Space Telescope¹. This may be due to the slight deviations within the mean magnitudes and periods of the Cepheid Variables. It should also be worth noting that seven of the Cepheids observed reside in the Cassiopeia constellation while the other four inhabit the Cygnus constellation. This means that if there happened to be a cloud covering either of these constellations at the time of observing (especially Cassiopeia), then it would cause problems with the data from some, if not all, the stars that reside in that area. To account for this, more observations could be made of each Cepheid Variable as well as observing more (different) stars that reside in differing areas of the night sky, to avoid problems with most of the data obtained on specific nights. However, care would be required due to the slewing of the telescope, so the viewing charts would need to be taken into account.

6.2 Andromeda Results

The period of 31.4 days derived for Andromeda *V1* is in almost full agreement with the period derived by Edwin Hubble in 1929 of 31.390 days¹³. The distance to Andromeda, determined to be $825 \pm 106 \text{ kpc}$, does also agree with the literature value from *Adam G. Riess et al.*, but to within $\sim 1\sigma$. However, due to the discrepancies in the Period-Luminosity relation discussed in section 6.1, the margin of error on the distance value determined is very large ($\sim 12\%$). This is most likely due to a lack of data for both the Cepheid Variable measurements and the Andromeda *V1* measurements. To get a more accurate and more precise value, the Cepheid *V1* would require to be observed for a much longer time period with much more data to work with, thus reducing the

error. Another source of error for *V1* comes from the matter of flux scaling with exposure time, and since *V1* is much further away, care needs to be taken when deciding on exposure times for the observations as to achieve a higher signal-to-noise ratio. The lower the signal-to-noise ratio, the higher the error becomes. A higher signal-to-noise can also be achieved by producing more images and stacking those images for greater clarity.

It is also worth mentioning that the data for the Andromeda observations was collected by a third party, who also performed the data reduction for this data. It is therefore unclear how the data reduction was performed and thus it is difficult to tell how successful the process was. Thus, the signal-to-noise ratio for each of the observations is unknown. The data itself is also quite limited due to a shorter period of observations, so it is difficult to tell whether the signal-to-noise ratio generated is sufficient to produce a precise estimate of the distance to Andromeda.

Finally, Andromeda *V1* proved to have a very large mean magnitude of ~ 19 in the V-Band of the UBVRI (Johnson-Cousins) system. This means that the Cepheid is very faint and thus extracting the magnitudes using the *Source Extractor* software package proved very difficult; and so to determine the $E(B-V)$ colour excess value, this had to be done manually using *GAIA* and manually defined aperture sizes. This causes a large source of systematic error within the colour excess. In addition to this, the R_V value of 3.1 was used to determine the dust extinction between the Earth and Andromeda, however, the 3.1 is the associated average R_V for the Milky Way Galaxy, and thus for Andromeda and the Intergalactic Medium, this value likely differs.

7. CONCLUSIONS

The intention of this project was to verify an intrinsic relationship between a Cepheid Variable Star's pulsation period and its bolometric luminosity, with the secondary aim of using this relationship to recreate the observation that Edwin Hubble performed in the early 19th century and determine the distance to the galaxy Messier-31, otherwise known as Andromeda. These objectives were achieved to varying degrees of accuracy, with the Period-Luminosity relation differing by $\sim 2\sigma$, whereas the distance differs by $< 1\sigma$, although with a much larger margin of error.

The mean apparent magnitudes of the targeted Cepheid Variables were measured, and after determining their absolute magnitude by correcting for extinction and using the distance modulus relation with the known distances, this was used to plot mean absolute magnitude-period (M-P). Some of these relations for the Cepheid Variables were observed to fit a sine curve, whereas others better fit a sawtooth graph. Their luminosity could then be found from the absolute magnitude to plot a Period-Luminosity (P-L) relation. This relation was found to have a rela-

tively clear trendline for the ten Cepheids. One star unfortunately had to be excluded due to difficulties in the period fitting for both the sawtooth model and the sine curve model. The mean apparent magnitude was found for Andromeda $V1$ and using the derived P-L relation, this value was added to the plot to extrapolate a value for the corresponding mean absolute (or ‘true’) magnitude, which was determined to be $M_{V1} = -5.619 \pm 1.565$. Using the distance modulus equation (equation 19), the absolute magnitude value was used to determine the distance to Andromeda, which was found to be $825 \pm 106\text{kpc}$. The primary objectives of this project were met, however, the degrees of accuracy and precision are far from ideal. These observations should be repeated over a longer observation period, using the methods discussed in section 6, to improve precision and accuracy to a more reasonable state.

Acknowledgements

First, we would like to thank the University of Edinburgh School of Physics and Astronomy for providing the necessary knowledge and skills required to complete this project, as well as the facilities required to perform the project. In particular, our supervisor - *Prof. P. N. Best, FRSE*, for the assistance and supervision throughout the duration of the project. We would also like to mention the time put in by the other Professors (Dr. C. Snodgrass - Telescope Group Project Course Organiser, Prof. R. J. McLure, and Dr. T. Dupuy) for the workshop presentations on how to analyse and work with our data. As well as the number of teaching assistants who kindly gave up their evenings to assist in the observations until late into the night, should anything have gone wrong.

Second, it is worth thanking the Open University for allowing the use of their private telescope (PIRATE) in the Canary Islands to gather our data.

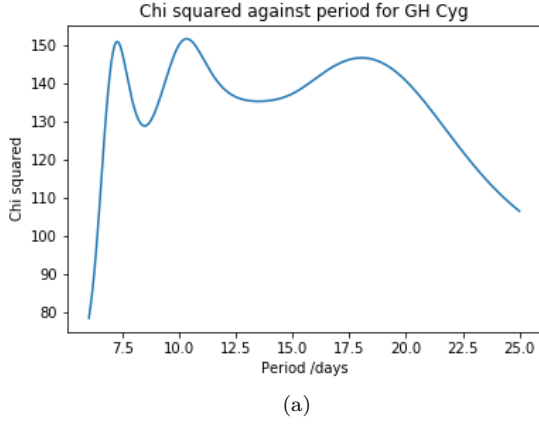
Finally, we should thank the team who used the Liverpool Telescope in Spain to gather observations of CV1 in Andromeda as we were unable to observe with the PIRATE telescope for a long enough period of time to gather sufficient data to determine the distance.

- ¹ G. Fritz Benedict, B. E. McArthur, L. W. Fredrick, T. E. Harrison, C. L. Slesnick, J. Rhee, R. J. Patterson, M. F. Skrutskie, O. G. Franz, L. H. Wasserman, W. H. Jefferys, E. Nelan, W. van Altena, P. J. Shelus, P. D. Hemenway, R. L. Duncombe, D. Story, A. L. Whipple, and A. J. Bradley. Astrometry with the [ITAL]hubble space telescope/[ITAL]: A parallax of the fundamental distance calibrator cephei. *The Astronomical Journal*, 124(3):1695–1705, sep 2002. doi:10.1086/342014. URL <https://doi.org/10.1086/342014>.
- ² Adam G. Riess, JÃ¼rgen Fliri, and David Valls-Gabaud. CEPHEID PERIOD-LUMINOSITY RELATIONS IN THE NEAR-INFRARED AND THE DISTANCE TO m31 FROM THEHUBBLE SPACE TELESCOPEWIDE FIELD CAMERA 3. *The Astrophysical Journal*, 745(2):156, jan 2012. doi:10.1088/0004-637x/745/2/156. URL <https://doi.org/10.1088/0004-637x/745/2/156>.
- ³ Edward Pigott. Vii. observations of a new variable star. in a letter from edward pigott, esq. to sir. h. c. englefield, bart. f.r.s. and a.s. *Philosophical Transactions of the Royal Society of London*, 75:127–136, 1785. doi:10.1098/rstl.1785.0007. URL <https://royalsocietypublishing.org/doi/abs/10.1098/rstl.1785.0007>.
- ⁴ John Goodricke. Ii. a series of observations on, and a discovery of, the period of the variation of the light of the star marked δ by bayer, near the head of cepheus. in a letter from john goodricke, esq. to nevil maskelyne, d.d. f. r. s. *Philosophical Transactions of the Royal Society of London*, 76:48–61, 1786. doi:10.1098/rstl.1786.0002. URL <https://royalsocietypublishing.org/doi/abs/10.1098/rstl.1786.0002>.
- ⁵ Henrietta S. Leavitt. 1777 variables in the Magellanic Clouds. *Annals of Harvard College Observatory*, 60:87–108.3, January 1908.
- ⁶ Henrietta S. Leavitt and Edward C. Pickering. Periods of 25 Variable Stars in the Small Magellanic Cloud. *Harvard College Observatory Circular*, 173:1–3, March 1912. URL <https://ui.adsabs.harvard.edu/abs/1912HarCi.173....1L>.
- ⁷ Rudolf Kippenhahn and Alfred Weigert. *Stellar Structure and Evolution*. 1994.
- ⁸ Alfred Gautschy and Hideyuki Saio. Stellar pulsations across the hr diagram: Part ii. *Annual Review of Astronomy and Astrophysics*, 34(1):551–606, 1996. doi:10.1146/annurev.astro.34.1.551. URL <https://doi.org/10.1146/annurev.astro.34.1.551>.
- ⁹ Lino Reggiani and Eleonora Alfinito. Stefan-boltzmann law revisited. 2022. doi:10.48550/arXiv.2112.12090.
- ¹⁰ G. P. Kuiper. The Empirical Mass-Luminosity Relation. *Astrophys. J.*, 88:472, November 1938. doi:10.1086/143999.
- ¹¹ M. Harwit. *Astrophysical Concepts*, pages 313–373. 4th edition, 1973. ISBN 978-0-387-96683-0. doi:10.1007/978-1-4757-2019-8.
- ¹² P. Kupperberg. *Hubble and the Big Bang*, pages 45–46. 2005. ISBN 978-1404203075.
- ¹³ E. P. Hubble. A spiral nebula as a stellar system, Messier 31. *Astrophys. J.*, 69:103–158, March 1929. doi:10.1086/143167.
- ¹⁴ Edwin Hubble. A relation between distance and radial velocity among extra-galactic nebulae. *Proceedings of the National Academy of Sciences*, 15(3):168–173, 1929. doi:10.1073/pnas.15.3.168. URL <https://www.pnas.org/doi/abs/10.1073/pnas.15.3.168>.
- ¹⁵ Robert P. Kirshner. Hubble's diagram and cosmic expansion. *Proceedings of the National Academy of Sciences*, 101(1):8–13, 2004. doi:10.1073/pnas.2536799100. URL <https://www.pnas.org/doi/abs/10.1073/pnas.2536799100>.
- ¹⁶ D. H. Smith. Eddington's Valve and Cepheid Pulsations. , 68:519, December 1984.
- ¹⁷ Wendy L. Freedman and Barry F. Madore. The hubble constant. *Annual Review of Astronomy and Astrophysics*, 48(1):673–710, Aug 2010. ISSN 1545-4282. doi:10.1146/annurev-astro-082708-101829. URL <http://dx.doi.org/10.1146/annurev-astro-082708-101829>.
- ¹⁸ M. Read. Image/Pixel-map Extraction [Online Software], August 2008. URL <http://www-wfau.roe.ac.uk/ssspixel.html>. Accessed: 03-03-2022.
- ¹⁹ C. A. Murray. The transformation of coordinates between the system of B1950.0 and J2000.0, and the principal galactic axes referred to J2000.0. , 218:325–329, July 1989. URL <https://ui.adsabs.harvard.edu/abs/1989A&A...218..325M>.
- ²⁰ I. N. Reid, C. Brewer, R. J. Brucato, W. R. McKinley, A. Maury, D. Mendenhall, J. R. Mould, J. Mueller, G. Neugebauer, J. Phinney, W. L. W. Sargent, J. Schombert, and R. Thicksten. The Second Palomar Sky Survey. , 103:661, July 1991. doi:10.1086/132866. URL <https://ui.adsabs.harvard.edu/abs/1991PASP..103..661R>.
- ²¹ PIRATE Observing Primer v3.4. The Open University, 2019.
- ²² Javier Méndez. Isaac Newton Group of Telescopes StarAlt Object Visibility Planner, 2019. URL <http://catserver.ing.iac.es/staralt/>. Accessed: 03-03-2022.
- ²³ Sybilla Technologies. URL <http://sybillatechnologies.com/>. Accessed: 03-03-2022.
- ²⁴ Frederick R. Chormey. *To Measure the Sky: An Introduction to Observational Astronomy*. Cambridge University Press, New York, 2010.
- ²⁵ A.C. Davenhall, G.J. Privett, and Taylor M.B. *The 2-D CCD Data Reduction Cookbook*. Council for the Central Laboratory of the Research Councils, August 2001.
- ²⁶ Medicals Telescopes Tools: FLI - ProLine Series - KAF-16803 Full Frame Front Illuminated Monochrome CCD Camera - 65mm Shutter. <https://tinyurl.com/medicopes>. Accessed: 03-03-2022.
- ²⁷ S. Holmes, U. Kolb, C. A. Haswell, V. Burwitz, R. J. Lucas, J. Rodriguez, S. M. Rolfe, J. Rostron, and J. Barker. PIRATE: A Remotely Operable Telescope Facility for Research and Education. , 123(908):1177, October 2011. doi:10.1086/662148. URL <https://ui.adsabs.harvard.edu/abs/2011PASP..123.1177H>.
- ²⁸ Michael Richmond. Dark Subtraction and Flatfielding, .
- ²⁹ Michael Richmond. Readout Noise, and Total Noise , .
- ³⁰ Thomas J. Fellers and Michael W. Davidson. Concepts in Digital Imaging Technology: CCD Noise Sources and Signal-to-Noise Ratio.
- ³¹ S. Littlefair. PHY217: L11: Detectors.
- ³² Note1. N. B. The calibrated frames of the Cepheid *V1* were stacked to create a deep image prior to normalising, whilst the images of the Cepheids were not.

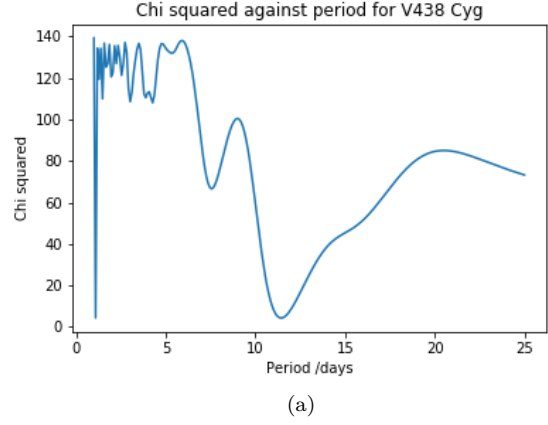
- ³³ Arlo U. Landolt. UVBRI Photometric Standard Stars Around the Celestial Equator: Updates and Additions. , 137(5):4186–4269, May 2009. doi:10.1088/0004-6256/137/5/4186.
- ³⁴ A.C. Davenhall and J. Palmer. *The CCD Photometric Calibration Cookbook*. Council for the Central Laboratory of the Research Councils, August 2001.
- ³⁵ Nigel Douglas. REDUCING CCD IMAGES.
- ³⁶ P. W. Draper. GAIA - Graphical Astronomy and Image Analysis Tool.
- ³⁷ R. Kron, H. Spinrad, G. Wirth, and S. McGaugh. Astronomical Magnitude Systems (Adapted from Observations of Distant Galaxies).
- ³⁸ Note2. The “meridian flip” is the movement undergone by the telescope wherein it rotates 180° to continue tracking an object after it has passed the meridian i.e. after reaching its peak altitude.
- ³⁹ Note3. The Cepheids were only imaged in the V-filter as it was only necessary to image Andromeda and the Standard Stars in both the B- and V-filter.
- ⁴⁰ Index to variable stars. <http://www.kusastro.kyoto-u.ac.jp/vsnet/gcvs2/index.html>. Accessed: 03-03-2022.
- ⁴¹ Y. Avni. Energy spectra of X-ray clusters of galaxies. *Astrophys. J.*, 210:642–646, December 1976. doi: 10.1086/154870.
- ⁴² Jason A. Cardelli, Geoffrey C. Clayton, and John S. Mathis. The Relationship between Infrared, Optical, and Ultraviolet Extinction. *Astrophys. J.*, 345:245, October 1989. doi:10.1086/167900.
- ⁴³ Cepheids - colour excess. https://www.astro.utoronto.ca/DDO/research/cepheids/table_colourexcess.html. Accessed: 03-03-2022.
- ⁴⁴ J. Allyn Smith, Douglas L. Tucker, Stephen Kent, Michael W. Richmond, Masataka Fukugita, Takashi Ichikawa, Shin-ichi Ichikawa, Anders M. Jorgensen, Alan Uomoto, James E. Gunn, Masaru Hamabe, Masaru Watanabe, Alin Tolea, Arne Henden, James Annis, Jeffrey R. Pier, Timothy A. McKay, Jon Brinkmann, Bing Chen, Jon Holtzman, Kazuhiro Shimasaku, and Donald G. York. The u'g'r'i'z' Standard-Star System. , 123(4):2121–2144, April 2002. doi:10.1086/339311.
- ⁴⁵ Sebastian Jester, Donald P. Schneider, Gordon T. Richards, Richard F. Green, Maarten Schmidt, Patrick B. Hall, Michael A. Strauss, Daniel E. Vanden Berk, Chris Stoughton, James E. Gunn, Jon Brinkmann, Stephen M. Kent, J. Allyn Smith, Douglas L. Tucker, and Brian Yanny. The Sloan Digital Sky Survey View of the Palomar-Green Bright Quasar Survey. , 130(3):873–895, September 2005. doi:10.1086/432466.

APPENDICES

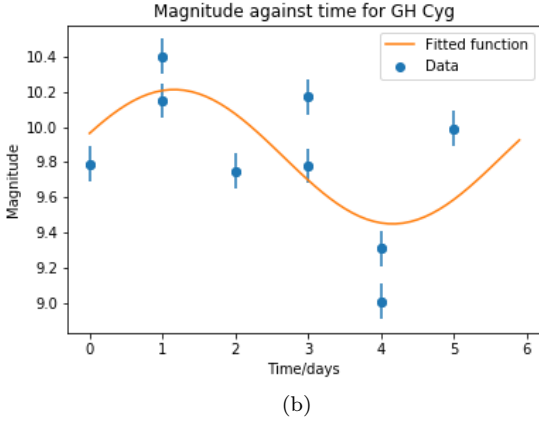
Appendix A: Cepheid Light-Curve fits



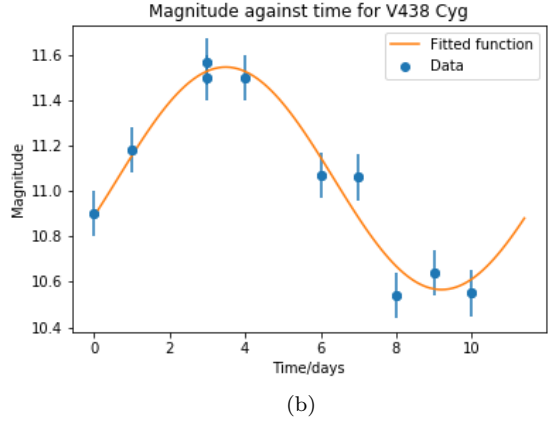
(a)



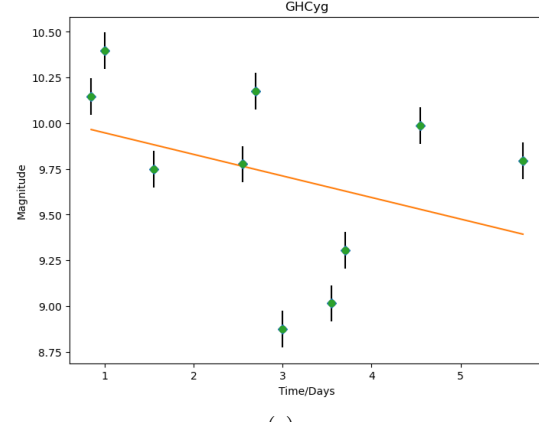
(a)



(b)

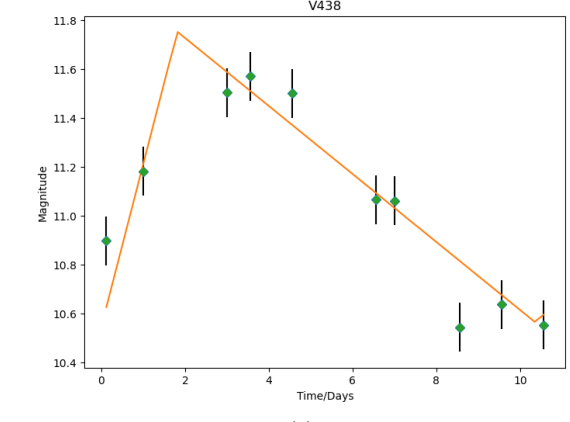


(b)



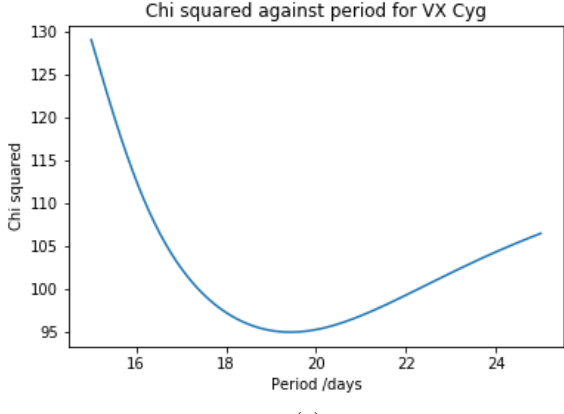
(c)

FIG. A.1: (a) χ^2 - period plot for GH Cyg (b) Sine curve fit for GH Cyg (c) Sawtooth fit for GH Cyg (note) Due to not being able to fit a decent light curve GH Cyg was rejected

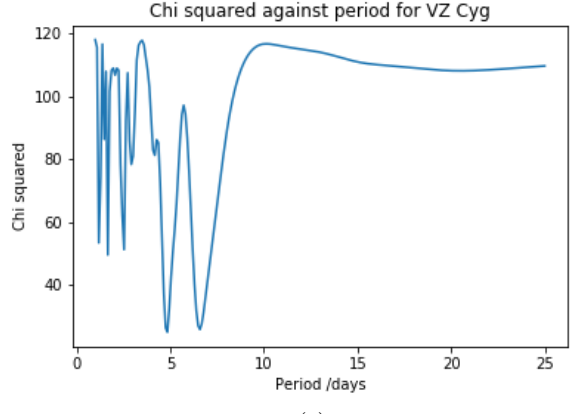


(c)

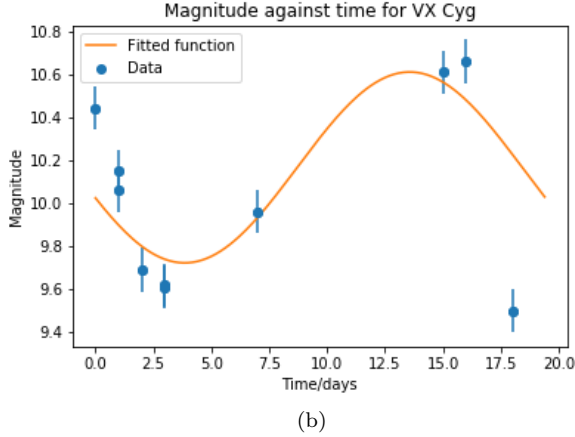
FIG. A.2: (a) χ^2 - period plot for V438 Cyg (b) Sine curve fit for V438 Cyg (c) Sawtooth fit for V438 Cyg (note) Used results from sawtooth fit



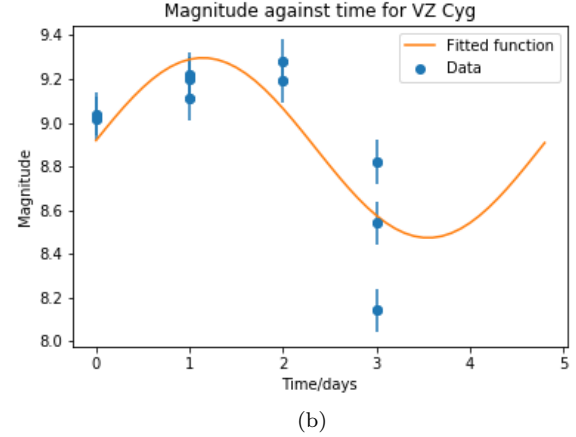
(a)



(a)

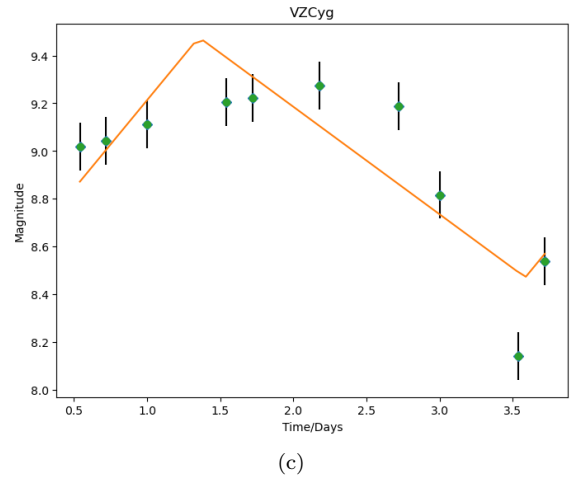


(b)



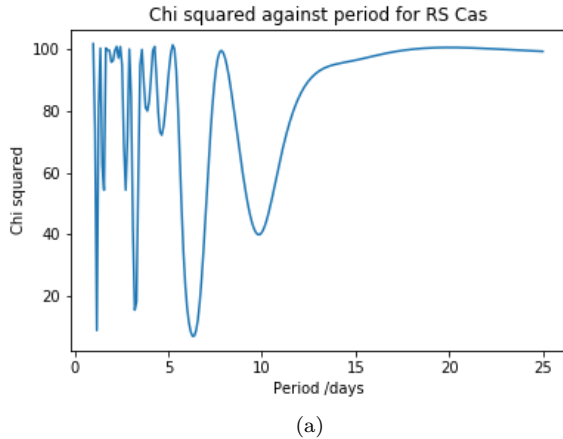
(b)

FIG. A.3: (a) χ^2 - period plot for VX Cyg (b) Sine curve fit for VX Cyg

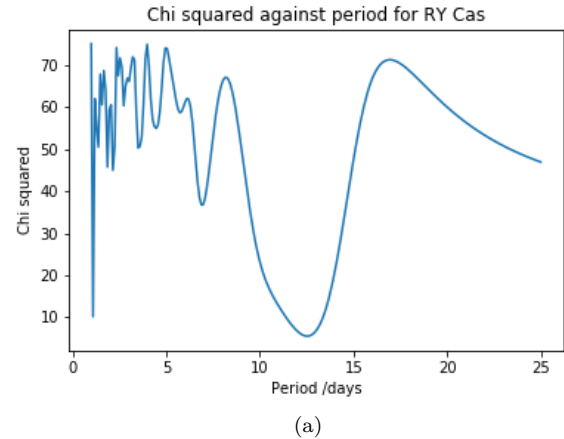


(c)

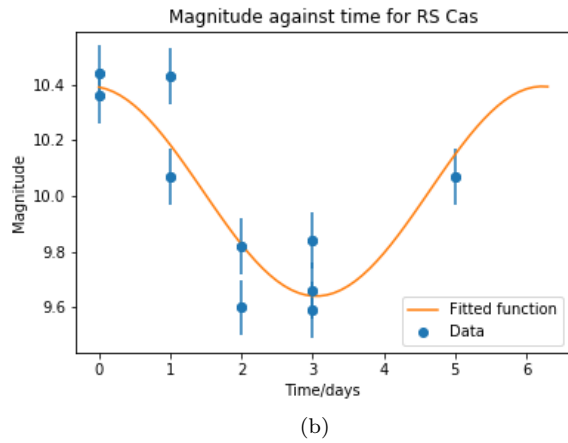
FIG. A.4: (a) χ^2 - period plot for VZ Cyg (b) Sine curve fit for VZ Cyg (c) Sawtooth fit for VZ Cyg (note) Used results from sawtooth fit



(a)

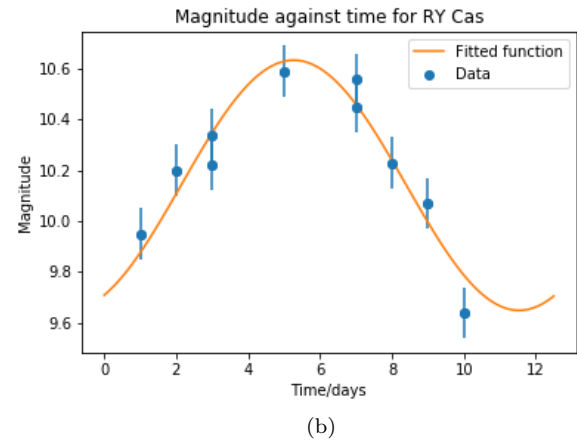


(a)



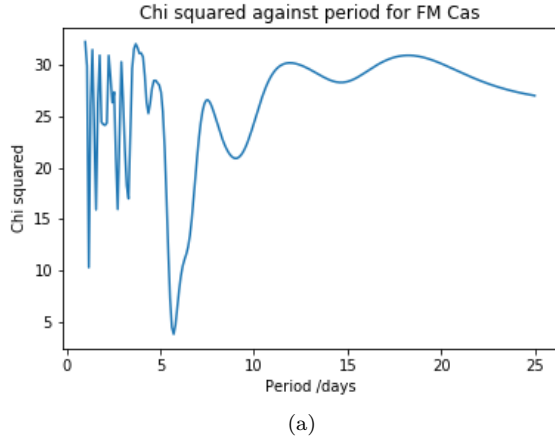
(b)

FIG. A.5: (a) χ^2 - period plot for RS Cas (b) Sine curve fit for RS Cas

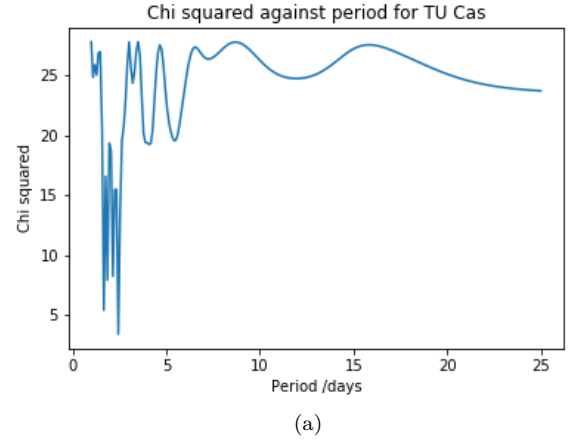


(b)

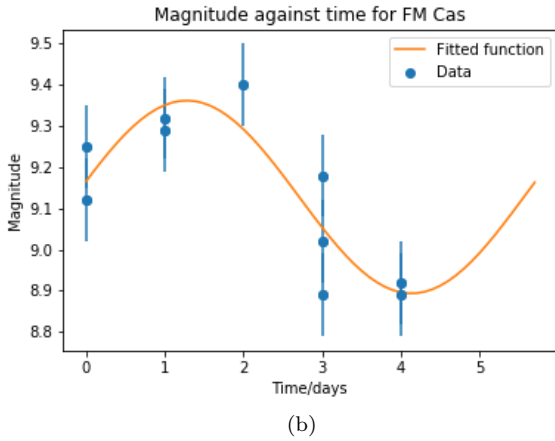
FIG. A.6: (a) χ^2 - period plot for RY Cas (b) Sine curve fit for RY Cas



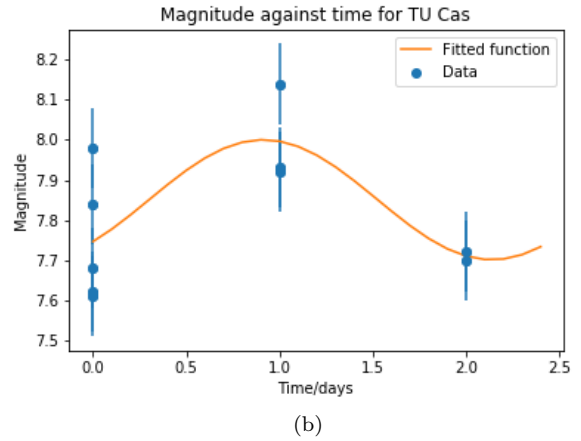
(a)



(a)

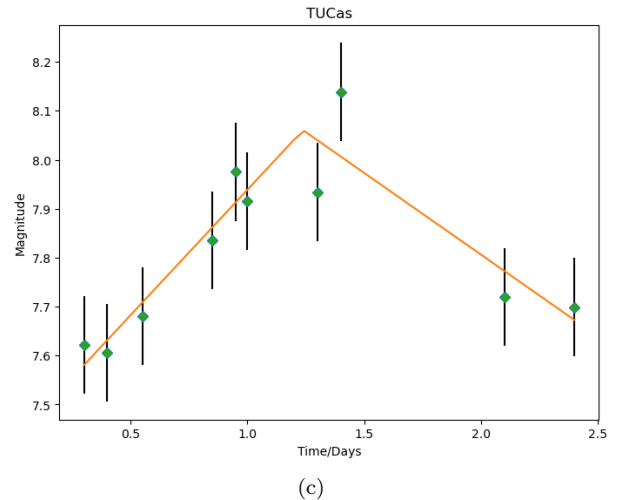


(b)



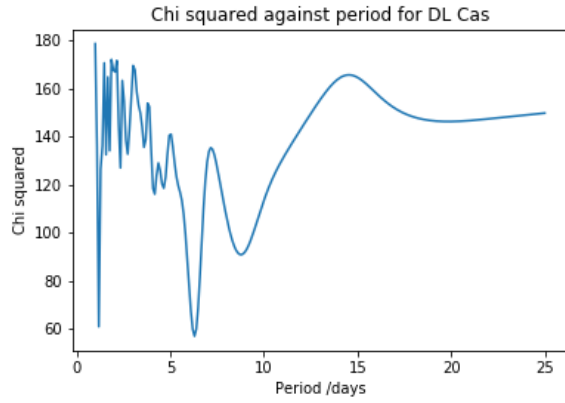
(b)

FIG. A.7: (a) χ^2 - period plot for FM Cas (b) Sine curve fit for FM Cas

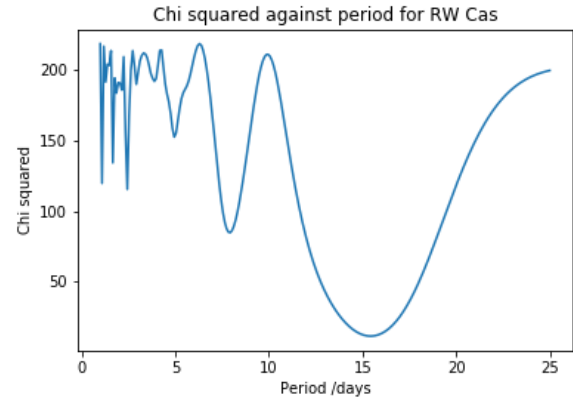


(c)

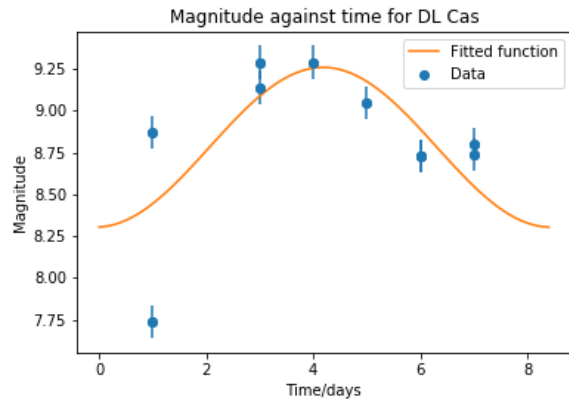
FIG. A.8: (a) χ^2 - period plot for TU Cas (b) Sine curve fit for TU Cas (c) Sawtooth fit for TU Cas (note) Used results from sawtooth fit



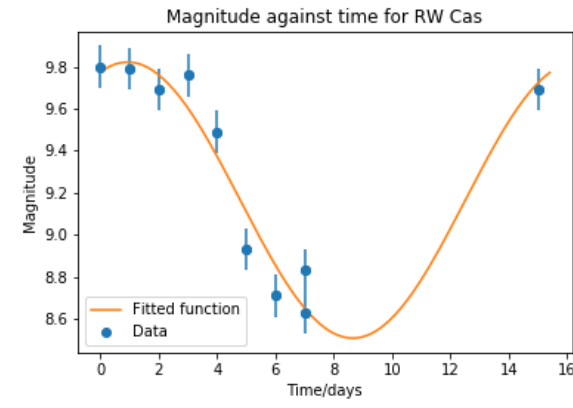
(a)



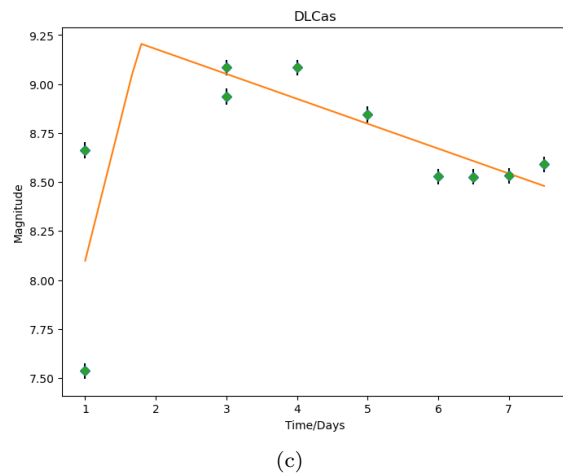
(a)



(b)



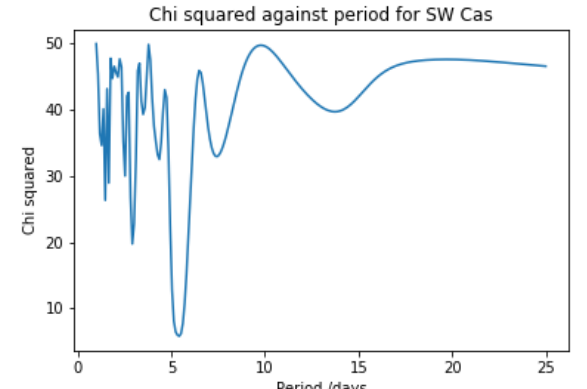
(b)



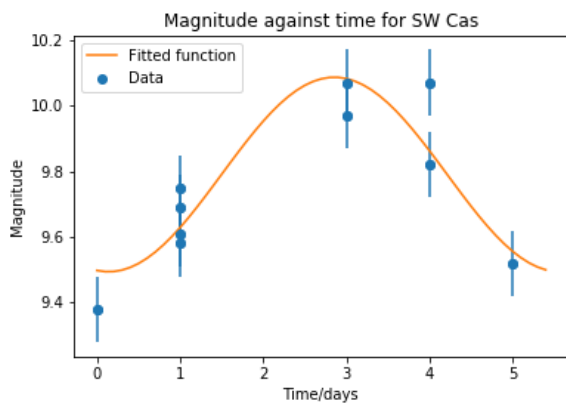
(c)

FIG. A.9: (a) χ^2 - period plot for DL Cas (b) Sine curve fit for DL Cas (c) Sawtooth fit for DL Cas (note) Used results from sawtooth fit

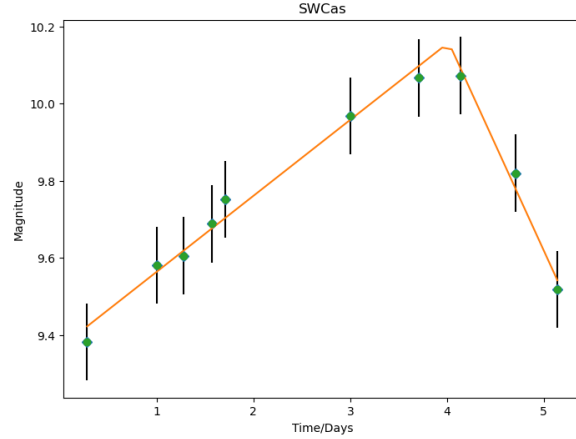
FIG. A.10: (a) χ^2 - period plot for RW Cas (b) Sine curve fit for RW Cas



(a)



(b)



(c)

FIG. A.11: (a) χ^2 - period plot for SW Cas (b) Sine curve fit for SW Cas (c) Sawtooth fit for SW Cas (note) Used results from sawtooth fit

Appendix B: Tables

TABLE B1: Cepheid Targets and their respective coordinates in the RA and DEC system^a

Cepheid Name	Right Ascension RA	Declination DEC
GH Cyg	19 59 10.80	+29 27 02.7
V438 Cyg	20 18 54.32	+40 03 52.2
VX Cyg	20 57 20.83	+40 10 39.1
VZ Cyg	21 51 41.44	+43 08 02.5
δ Cep	22 29 10.26	+58 24 54.7
RS Cas	23 37 16.06	+62 25 44.4
RY Cas	23 52 07.03	+58 44 30.2
FM Cas	00 14 28.24	+56 15 10.6
TU Cas	00 26 19.45	+51 16 49.3
DL Cas	00 29 58.59	+60 12 43.1
RW Cas	01 37 14.02	+57 45 33.2
SW Cas	23 07 10.08	+58 33 15.1
Andromeda CV1	00 41 27.30	+41 10 10.4

^a N.B. GH Cyg was excluded due to problems, and δ Cep was replaced by SW Cas due to oversaturation.

TABLE B2: Cepheids and their measured periods and uncertainties

Cepheid Name	Period (days)	Negative Error (days)	Positive Error (days)	Literature Period ⁴⁰ (days)
V438 Cyg	11.44	0.23	0.26	11.21
VX Cyg	19.43	0.93	1.07	20.13
VZ Cyg	4.82	0.06	0.06	4.86
RS Cas	6.35	0.11	0.11	6.30
RY Cas	12.53	0.48	0.42	12.14
FM Cas	5.71	0.11	0.11	5.81
TU Cas	2.45	0.025	0.025	2.14
DL Cas	8.79	0.29	0.29	8.00
RW Cas	15.43	0.43	0.40	14.79
SW Cas	5.43	0.23	0.16	5.44

TABLE B3: Cepheids and their measured apparent magnitudes, dust correction and absolute magnitudes

Cepheid Name	Mean Apparent Magnitude	Literature App Mag ⁴⁰	$E(B-V)^{43}$	A_V	Dust Corrected App Mag	Absolute Magnitude
V438 Cyg	11.14	12-13.50	1.13	3.50	7.64	-4.05
VX Cyg	10.20	9.54-10.55	0.79	2.45	7.75	-4.86
VZ Cyg	9.00	8.6-9.28	0.29	0.90	8.10	-3.16
RS Cas	9.65	9.53-10.36	0.88	2.73	6.92	-3.82
RY Cas	10.15	9.38-10.39	0.65	2.02	8.14	-4.78
FM Cas	9.13	8.82-9.47	0.31	0.96	8.17	-3.29
TU Cas	7.84	6.88-8.18	0.12	0.37	7.47	-2.07
DL Cas	8.98	8.63-9.26	0.53	1.64	7.34	-3.80
RW Cas	9.15	8.62-9.76	0.42	1.30	7.85	-4.57
SW Cas	9.8	9.32-10.01	0.49	1.52	8.28	-3.23